Chapter 1

MIRA – Physical Layer Optimisation for the Multiband Impulse Radio UWB Architecture

Rainer Moorfeld, Adolf Finger, Hanns-Ulrich Dehner, Holger Jäkel, Martin Braun and Friedrich K. Jondral

Additional information is available at the end of the chapter

http://dx.doi.org/10.5772/55076

1. Introduction

Future wireless communication systems have to be realised in a simple and energy efficient manner while guaranteeing sufficient performance. Furthermore, the available frequency resources have to be used flexibly and efficiently. In this context two different approaches have been considered in recent years: On one hand OFDM-based overlay systems in which a primary user dynamically allocates unused frequencies to one or more secondary users [57] and on the other hand unlicensed, easy-to-realise and low-cost ultra-wideband (UWB) systems. This underlying technology operates with an extremely low transmission power over a wide frequency range and does not interfere with existing licensed systems [15].

In order to establish UWB on the consumer market it has to get along with some challenges. Such challenges are, e.g., the realisation of practical, low-complex and energy-efficient transceiver architectures, the investigation of methods for accurate synchronization and channel estimation or the handling of high sample rates. To meet these requirements this chapter considers a non-coherent multiband impulse radio UWB (MIR-UWB) system [11, 45, 46]. The MIR-UWB system focuses on short-range high data rate communication applications. The MIR-UWB system is an alternative to the architectures Multiband OFDM UWB [2] and Direct Sequence UWB [16] which have been proposed within the IEEE 802.15.3a standardization process.

The chapter is organised as follows: Section 2 gives a short introduction into the physical layer architecture of the non-coherent MIR-UWB system. In the following section 3 the performance of the energy detection receiver is analysed with respect to different aspects. In contrast section 4 deals with interference investigations for the non-coherent MIR-UWB system aiming at an efficient and intelligent interference handling. The chapter concludes with section 5 in which a summary is given.

INTECH
open science | open minds

©2013 Dehner et al., licensee InTech. This is an open access chapter distributed under the terms of the Creative Commons Attribution License (http://creativecommons.org/licenses/by/3.0), which permits unrestricted use, distribution, and reproduction in any medium, provided the original work is properly cited.

2. Multiband impulse radio

The idea of the MIR-UWB architecture is based on [45, 46]. The architecture proposed there comprises a transmitter using multiple bands and impulse radio within the bands to transmit data and a receiver, which detects only the energy of the transmitted impulses. The combination of energy detection receiver and multiband enables a flexible high data rate system with low power consumption.

2.1. Transmitter

The MIR-UWB transmitter is based on a multiband pulse generation followed by a modulator. The multiband pulse generator generates a pulse with a specified bandwidth for every subband. Subbands can be activated or deactivated using the bandplan. Different possibilities to generate theses pulses are shown in [30]. Each subband pulse will be modulated with different data, all subband pulses are summed up to a multiband pulse, amplified and transmitted. Figure 1 shows a transmitter based on an *oscillator bank* pulse generator.

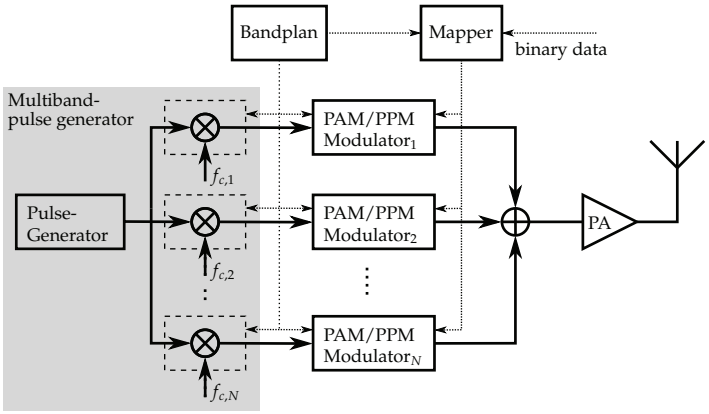

Figure 1. MIR-UWB Transmitter based on *oscillator bank* pulse generation

2.2. Receiver

The MIR-UWB receiver is based on N parallel energy detection receivers. A filter bank separates the individual subband pulses and an energy detector measures the energy in every subband. Based on the measured energy, the demodulator makes his decision. For pulse amplitude modulation (PAM) and its special case of on-off-keying (OOK) the demodulation process needs to know the SNR in each subband. This can be estimated using a preamble [46]. The channel state information can be used for Detect and Avoid (DAA) algorithms [34] and to increase the performance of the multiband system [28]. Pulse position modulation (PPM) and transmit reference (TR) do not need any channel state information.

3. Energy detection

The MIR-UWB architecture is based on energy detection. Thus the receiver detects *only* the energy of the received signal in a specified window. The disadvantage in performance is

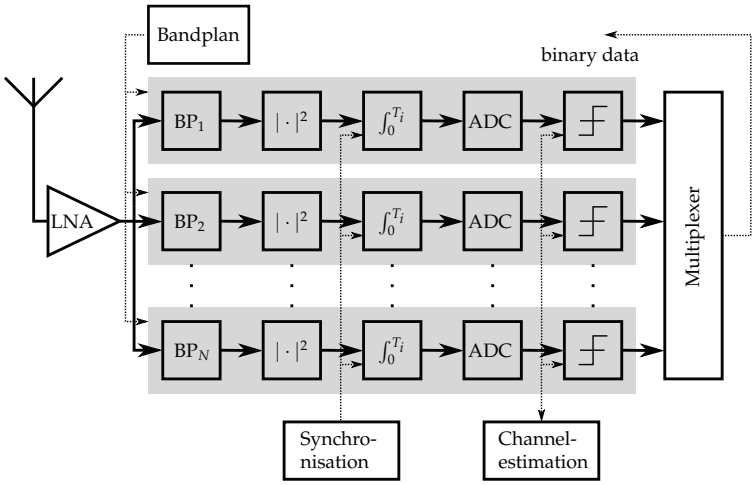

Figure 2. MIR-UWB receiver

accompanied by a very simple receiver design [36, 38, 54]. The performance measure is based on the average symbol error probability (SEP) or bit error probability (BEP) and will be derived in the following section.

3.1. Demodulation

In the additive white gaussian noise (AWGN) channel the received signal R is the sum of the transmitted signal s and white Gaussian noise W with the power spectral density of $N_0/2$:

$$R(t) = s(t) + W(t) = a_m p(t) + W(t). \tag{1}$$

The transmitted signal s is a weighted pulse p. The amplitude of the pulse is a_m. Thus, the energy of a transmitted signal is:

$$\begin{aligned} E_S &= \int_{t_0}^{t_0+T_i} s^2(t)\,\mathrm{d}t = a_m^2 \int_{t_0}^{t_0+T_i} p^2(t)\,\mathrm{d}t \\ &= \sum_{i=1}^{2D} s_i = a_m^2 \sum_{i=1}^{2D} p_i, \end{aligned}$$

where $s_i := s(i/(2B))$ and $p_i := p(i/(2B))$ and B denoting the bandwidth. The received energy can be approximated by a finite sum of $2D = 2T_iB$ samples [56]. The event $\{A = a_m\}$ with the range $\mathcal{A} = \{a_0, \ldots, a_{M-1}\}$ describes a transmitted symbol with the amplitude a_m. Without loss of generality the integration starts at $t_0 = 0$. In order to measure the energy, the detector squares the received signal $R(t)$ and integrates the result over the time interval T_i. The received energy, normalized by the power spectral density $N_0/2$, is:

$$Y = \frac{2}{N_0} \int_0^{T_i} R^2(t)\,\mathrm{d}t. \tag{2}$$

A time discrete representation of the received energy Y is:

$$Y = \frac{1}{N_0 B} \sum_{i=1}^{2D} (s_i + W_i)^2 , \tag{3}$$

where $W_i := W(i/(2B))$. If the symbol energy is $E_S = 0$, the received energy Y will be χ^2 distributed with the degree of freedom of $2D$. If the symbol energy $E_S > 0$, the received energy will be noncentral χ^2 distributed with the degree of freedom of $2D$ and the noncentrality parameter μ:

$$\mu = \sum_{i=1}^{2D} s_i^2 = \frac{2}{N_0} \int_0^T s^2(t)\,\mathrm{d}t =: \frac{2E_s}{N_0} = 2\gamma, \tag{4}$$

where $\gamma = E_S/N_0$ is the SNR at the receiver. Thus, the distribution of the received energy Y depends on the symbol energy E_S:

$$Y \sim \begin{cases} \chi^2_{2D} & \text{for } E_S = 0 \\ \chi^2_{2D}(2\gamma) & \text{for } E_S > 0 \,. \end{cases}$$

The conditional probability density function $f_{Y|A}(\cdot|a_0)$ with $a_0 = 0$ and $E_S = 0$ of the received energy Y is:

$$f_{Y|A}(y|a_0) = \frac{1}{2^D \Gamma(D)} y^{D-1} \exp\left(-\frac{y}{2}\right). \tag{5}$$

The conditional probability density function $f_{Y|A}(\cdot|a_m)$ with $a_m > 0$ and $E_S > 0$ of the received energy Y is:

$$f_{Y|A}(y|a_m) = \frac{1}{2}\left(\frac{y}{2\gamma}\right)^{\frac{D-1}{2}} \exp\left(-\frac{2\gamma + y}{2}\right) \mathrm{I}_{D-1}\left(\sqrt{2\gamma y}\right), \tag{6}$$

where Γ is the gamma function [18, eq. 8.310.1] and I_n is the modified Bessel function of the first kind of order n [1, eq. 9.6.3].

3.2. AWGN channel

First we calculate the bit error probability of the energy detection receiver in the AWGN channel (1). This receiver detects only the energy of the received signal (2), (3).

3.2.1. Pulse amplitude modulation

The M-PAM modulated signal is:

$$s(t) = \sum_{k=-\infty}^{\infty} a_{m,k} p(t - kT_r)$$

and transmits $\log_2(M)$ bit per symbol. The energy of the m^{th} symbol is:

$$E_{S_m} = \underbrace{\int_0^{T_i} s^2(t)\,\mathrm{d}t}_{=\sum_{i=1}^{2D} s_i^2} = a_m^2 \underbrace{\int_0^{T_i} p^2(t)\,\mathrm{d}t}_{=\sum_{i=1}^{2D} p_i^2} = a_m^2 E_p,$$

where E_p is the energy of an unmodulated pulse p. The demodulator has to decide, which symbol m with the energy E_{S_m} and the amplitude a_m has been transmitted, based on the observation of the random variable Y. The optimal receiver, i. e. the receiver with the lowest probability to make a wrong decision, makes the decision for the symbol that has been sent most likely, given a certain energy y at the receiver. Thus, the receiver makes the decision for the symbol m with the amplitude a_m, when [25]:

$$\mathbb{P}\{A = a_m | Y = y\} \geq \mathbb{P}\{A = a_k | Y = y\}, \quad \forall\, m \neq k. \tag{7}$$

This is the maximum a posteriori probability (MAP) decision rule. If all transmitted symbols are equal probable, it can be reduced to the maximum-likelihood (ML) decision rule:

$$f_{Y|A}(y|a_m) \geq f_{Y|A}(y|a_k), \quad \forall\, m \neq k,$$

using the Bayes theorem:

$$\mathbb{P}(A = a_m | Y = y) = \frac{f_{Y|A}(y|a_m)\mathbb{P}(A = a_m)}{f_Y(y)} = \frac{f_{Y|A}(y|a_m)1/M}{f_Y(y)},$$

because $\mathbb{P}(A = a_m) = 1/M$ for all $m \in \{0, 1, \ldots, M-1\}$ and $f_Y(y)$ are independent of m. For the M-PAM modulated signal, we use the ML receiver with multiple hypothesis testing:

$$m = \underset{k \in [0, M-1]}{\arg\max}\, f_{Y|A}(y|a_k), \tag{8}$$

with the conditional probability density function $f_{Y|A}$ based on (5) and (6).

The SEP P_e for the energy detection receiver in the AWGN channel with M-PAM signals can be calculated as:

$$\begin{aligned} P_e(\overline{\gamma}, \mathbf{a}, \boldsymbol{\rho}, D) &= 1 - P_c(\overline{\gamma}, \mathbf{a}, \boldsymbol{\rho}, D) \\ &= 1 - \sum_{m=0}^{M-1} \mathbb{P}(\rho_m \leq Y < \rho_{m+1} | A = a_m)\mathbb{P}(A = a_m), \end{aligned} \tag{9}$$

where P_c is the probability of a correct decision and $\mathbb{P}(\rho_m < Y \leq \rho_{m+1} | A = a_m)$ is the conditional probability, that the received energy Y is in the interval $[\rho_m, \rho_{m+1})$, with the optimal interval thresholds ρ. Thus, the decision has been made using the ML decision rule (8). $\mathbb{P}(A = a_m)$ is the a priori probability, that the symbol m has been sent and $\mathbb{P}(A = a_m) = 1/M$ for all $m \in \{0, 1, \ldots, M-1\}$. The conditional probability $\mathbb{P}(\rho_m \leq Y < \rho_{m+1} | A = a_m)$ is:

$$\begin{aligned} \mathbb{P}(\rho_m < y \leq \rho_{m+1} | A = a_m) &= \int_{\rho_m}^{\rho_{m+1}} f_{Y|A}(y|a_m)\, \mathrm{d}y \\ &= F_{Y|A}(\rho_{m+1}|a_m) - F_{Y|A}(\rho_m|a_m). \end{aligned} \tag{10}$$

The related distribution function $F_{Y|A}(\cdot|0)$ can be calculated in closed form:

$$F_{Y|A}(y|0) = \int_0^y \frac{1}{2^D \Gamma(D)} u^{D-1} \exp\left(-\frac{u}{2}\right) \mathrm{d}u = \frac{\Gamma\left(D, \frac{y}{2}\right)}{\Gamma(D)}, \tag{11}$$

where $\Gamma(\cdot)$ is the Gamma function [18, eq. 8.310.1] and $\Gamma(\cdot,\cdot)$ is the incomplete Gamma function [18, eq. 8.350.1]. The distribution function (11) can be also displayed with the help of the Marcum-$\mathcal{Q}$ function:

$$\mathcal{Q}_m(a,b) = \int_b^\infty x \left(\frac{x}{a}\right)^{m-1} \exp\left(-\frac{x^2+a^2}{2}\right) \mathrm{I}_{m-1}(ax)\ \mathrm{d}x, \tag{12}$$

where I_n is the modified Bessel function of the first kind of order n [1, eq. 9.6.3]. Thus, an alternative representation for the distribution function (11) is for $D \in \mathbb{Z}^+$ with [49, eq. 2.1.124] and [52, eq. 4.71]:

$$F_{Y|A}(y|0) = 1 - \mathcal{Q}_D(0, \sqrt{y}). \tag{13}$$

If a symbol with an amplitude $a_m > 0$ has been sent, the conditional probability density function $f_{Y|A}(\cdot|a_m)$ has the form (6). There does not exist a closed form for the distribution function in general. But for $D \in \mathbb{Z}^+$ it can also be solved in closed form with the help of the Marcum-$\mathcal{Q}$ function (12):

$$\begin{aligned} F_{Y|A}(y|a_m) &= \int_0^y \frac{1}{2} \left(\frac{u}{2a_m^2\gamma}\right)^{\frac{D-1}{2}} \exp\left(-\frac{2a_m^2\gamma + u}{2}\right) \mathrm{I}_{D-1}\left(\sqrt{2a_m^2\gamma u}\right)\ \mathrm{d}u \\ &= 1 - \mathcal{Q}_D\left(a_m\sqrt{2\gamma}, \sqrt{y}\right). \end{aligned} \tag{14}$$

Combining (13) and (14) with (9), the SEP P_e for an energy detection receiver with M-PAM for an SNR of $\gamma = E_p/N_0$ is [35]:

$$P_e(\gamma, \mathbf{a}, \boldsymbol{\rho}, M, D) = 1 - \frac{1}{M}\left[\sum_{m=0}^{M-1} \mathcal{Q}_D\left(a_m\sqrt{2\gamma}, \sqrt{\rho_{m+1}}\right) - \mathcal{Q}_D\left(a_m\sqrt{2\gamma}, \sqrt{\rho_m}\right)\right] \tag{15}$$

with the M symbol amplitudes $\boldsymbol{a} = (a_0, a_1, \ldots, a_{M-2}, a_{M-1})$, $M+1$ interval thresholds $\boldsymbol{\rho} = (\rho_0, \rho_1, \ldots, \rho_{M-1}, \rho_M)$ and the degree of freedom $2D$. Applying the interval thresholds $\rho_0 = 0$ und $\rho_M \to \infty$, we get $\mathcal{Q}_D\left(a_m\sqrt{2\gamma}, \sqrt{\rho_0}\right) = 0$ and $\mathcal{Q}_D\left(a_m\sqrt{2\gamma}, \sqrt{\rho_M}\right) = 1$. Combining this with (15), it reduces to:

$$P_e(\gamma, \mathbf{a}, \boldsymbol{\rho}, M, D) = \frac{1}{M}\left[M - 1 + \sum_{m=1}^{M-1} \mathcal{Q}_D\left(a_m\sqrt{2\gamma}, \sqrt{\rho_m}\right) - \sum_{m=0}^{M-2} \mathcal{Q}_D\left(a_m\sqrt{2\gamma}, \sqrt{\rho_{m+1}}\right)\right]. \tag{16}$$

Figure 3 shows the influence of different degrees of freedom on the BEP of an energy detection receiver with OOK and 2-PPM. For large degrees of freedom, a higher SNR is necessary to achieve the same BEP. This is due to an increasing amount of noise at the detector. OOK shows a slightly better performance than 2-PPM. Figure 4 shows the influence of higher order modulation on the BEP.

3.2.1.1. Optimal interval thresholds

The optimal interval thresholds to minimise the SEP have to fulfil the following optimisation problem:

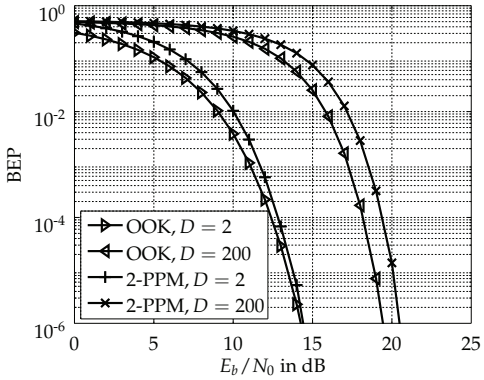

Figure 3. BEP for OOK and 2-PPM with different degrees of freedom

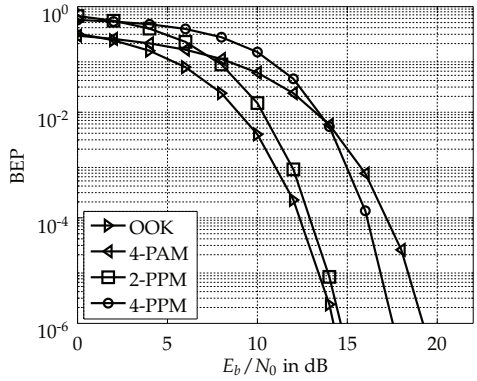

Figure 4. BEP for multilevel M-PAM and M-PPM for $D = 2$

$$\begin{aligned} \underset{\boldsymbol{\rho}}{\text{minimise}} \quad & P_e(\gamma, \boldsymbol{a}, \boldsymbol{\rho}, M, D) \\ \text{subject to} \quad & \frac{1}{M} \sum_{m=0}^{M-1} a_m^2 = 1, \end{aligned}$$

Thus, the optimal interval threshold ρ_{opt} between the two symbol amplitudes a_m and a_{m+1} has to fulfil the following equation:

$$f_{Y|A}(\rho_{\text{opt}}|a_m) = f_{Y|A}(\rho_{\text{opt}}|a_{m+1}), \tag{17}$$

where $f_{Y|A}$ are the conditional probability density functions based on (5) and (6). With these optimal interval thresholds, the symbol decision is based on the ML-criteria (8). Unfortunately, there is no closed form solution for determining the optimal interval thresholds. Thus, they have to be calculated numerically. Figure 5 shows the conditional probability density functions with equidistant symbol amplitudes a_m and optimal interval thresholds ρ_1, ρ_2 and ρ_3 with an SNR of $\gamma = 10\,\text{dB}$.

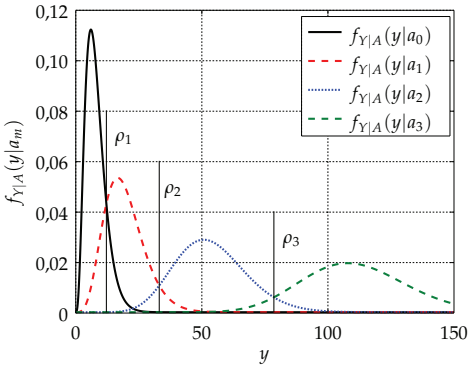

Figure 5. Optimal interval thresholds for 4-PAM ($\gamma = 10\,\text{dB}$)

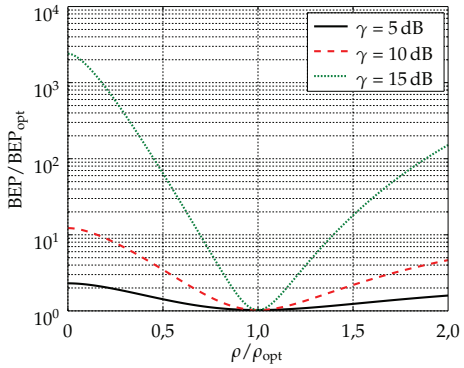

Figure 6. Sensitivity of the BEP related to the interval threshold ρ_1 for OOK

Figure 6 shows the influence of a non optimal interval threshold ρ_1 on the SEP for OOK ($M = 2$). In such a case, the SEP gets more sensitive for high SNR.

3.2.1.2. Optimal amplitudes

Now we try to minimise the SEP by optimising the symbol amplitudes $\boldsymbol{a}$. The optimisation problem is now [33, 37]:

$$\begin{aligned} \underset{\boldsymbol{a}}{\text{minimise}} \quad & P_e(\gamma, \boldsymbol{a}, \boldsymbol{\rho}, M, D) \\ \text{subject to} \quad & \frac{1}{M}\sum_{m=0}^{M-1} a_m^2 = 1, \end{aligned}$$

This optimisation problem can only be solved numerically, because the optimal interval thresholds $\boldsymbol{\rho}$ are based on the amplitudes $\boldsymbol{a}$ and there exists no closed form solution for the optimal interval thresholds $\boldsymbol{\rho}$ (17). For OOK ($M = 2$) the optimal amplitudes are $\boldsymbol{a}_{\text{opt}} = (0, 2)$. In this case they are independent of the SNR γ. For $M > 2$ it is possible to calculate a set of optimal amplitudes $\boldsymbol{a}_{\text{opt}}$ for every SNR γ. Figure 7 shows the SEP for 4-PAM for different symbol amplitudes a_1 and a_2 for a SNR of 16 dB. For figure 7 the amplitudes $a_0 = 0$ and

$a_3 = 1$ are set. The minimal SEP has been reached for $\boldsymbol{a} = (0, 0.35, 0.67, 1)$. Figure 8 shows

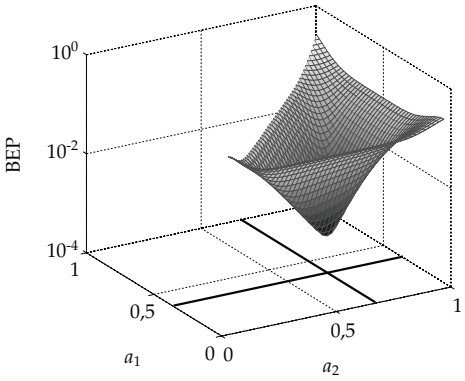

Figure 7. SEP for 4-PAM with different interval thresholds

the gain for 4-PAM with optimal amplitudes for different degrees of freedom. The results show impressive gains for large degrees of freedom. Figure 9 shows the optimal amplitudes for different degrees of freedom. For $D = 2$ the amplitudes are almost equidistant but for $D = 200$ the amplitudes are adjusted and not equidistant any more.

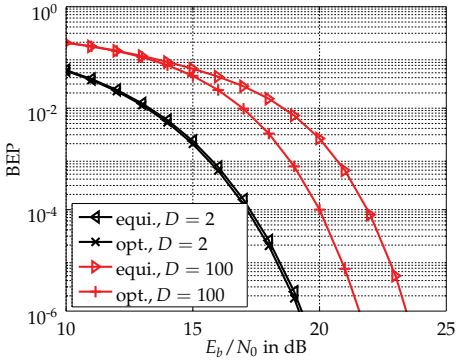

Figure 8. BEP for 4-PAM with equidistant and optimal amplitudes

3.3. Flat fading channel

To analyse the performance of an energy detection receiver we need a channel model that enables a good approximation of the energy at the receiver. Investigations of the IEEE channel model (802.15.3a) show that the energy at the receiver can be approximated by a random variable which is constant for one symbol.

Figure 10 compares the channel's magnitude (denoted as CIR) to a moving average of width 100 MHz and 1 GHz of the energy in the IEEE channel model. Figure 11 shows the magnitude at the receiver for a detector with 100 MHz and 1 GHz bandwidth. Thus we can use the

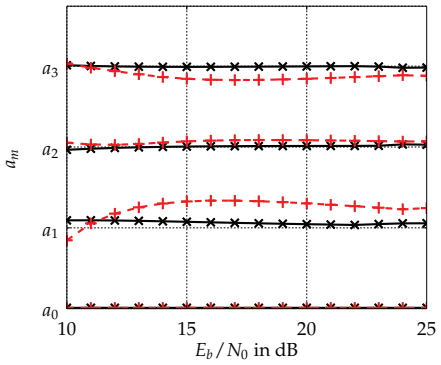

Figure 9. Optimal amplitudes for different degrees of freedom ($D = 2$, $D = 200$)

flat fading channel model to model the energy at the receiver in a frequency selective fading channel.

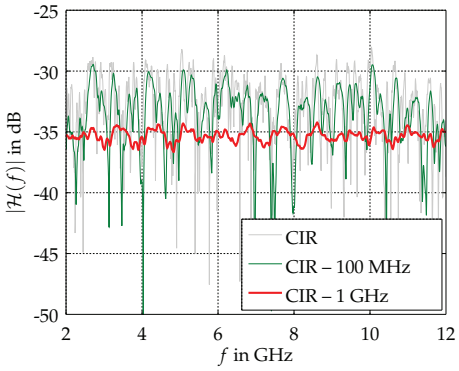

Figure 10. Moving average of the energy at the receiver (IEEE 802.15.3a, CM1)

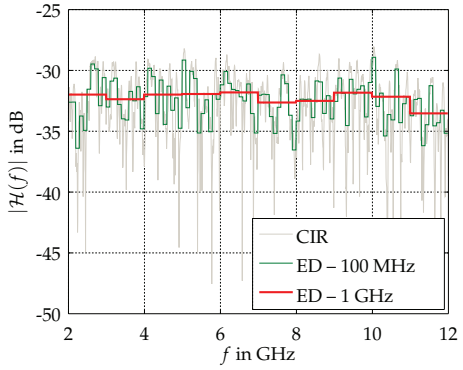

Figure 11. Energy at the receiver for different bandwidth (IEEE 802.15.3a, CM1)

In a flat fading channel, the random path attenuation H is assumed to be constant for the duration of a symbol. Thus, the received signal $R(t)$ in the interval $0 \leq t \leq T_S$ is:

$$R(t) = Hs(t) + W(t),$$

where $W(t)$ denotes the additive white Gaussian noise (AWGN) with a spectral power density of $N_0/2$.

The instantaneous SNR γ in the flat fading channel is:

$$\gamma = h^2 \frac{E_S}{N_0},$$

where h denotes the instantaneous path attenuation and E_S denotes the symbol energy. Since the SNR γ is random, γ is a realization of a a random variable Γ. The average SNR $\overline{\gamma}$ can be calculated using the expectation of the random variable H^2:

$$\overline{\gamma} = \Omega \frac{\overline{E_S}}{N_0} = \int_0^\infty \gamma f_\Gamma(\gamma)\, \mathrm{d}\gamma$$

with $\Omega = \mathbb{E}(H^2)$. Introducing a change of variable, the probability density function of the random variable Γ is [52, eq. 2.3]:

$$f_\Gamma(\gamma) = \frac{f_H(\sqrt{\frac{\Omega\gamma}{\overline{\gamma}}})}{2\sqrt{\frac{\gamma\overline{\gamma}}{\Omega}}}. \tag{18}$$

To calculate the average SEP in a flat fading channel, we have to solve the following integral [52, eq. 1.8]:

$$\overline{P}_e(\overline{\gamma}) = \int_0^\infty P_{e,AWGN}(\gamma) f_\Gamma(\gamma)\, \mathrm{d}\gamma. \tag{19}$$

3.3.1. Pulse amplitude modulation

Using the SEP in the AWGN channel (16) and the probability density function of the random SNR Γ in the flat fading channel, the average SEP for M-PAM is:

$$\begin{aligned}\overline{P}_e(\overline{\gamma}, \boldsymbol{a}, \boldsymbol{\rho}, M, D) = \frac{1}{M}\Bigg[& M - 1 - \mathcal{Q}_D\left(0, \sqrt{\rho_1}\right) \\ & + \sum_{m=1}^{M-1} \int_0^\infty \mathcal{Q}_D\left(a_m\sqrt{2\gamma}, \sqrt{\rho_m}\right) f_\Gamma(\gamma)\, \mathrm{d}\gamma \\ & - \sum_{m=1}^{M-2} \int_0^\infty \mathcal{Q}_D\left(a_m\sqrt{2\gamma}, \sqrt{\rho_{m+1}}\right) f_\Gamma(\gamma)\, \mathrm{d}\gamma \Bigg],\end{aligned} \tag{20}$$

with the symbol amplitudes $\boldsymbol{a} = (a_0, a_1, \ldots, a_{M-2}, a_{M-1})$ and the interval thresholds $\boldsymbol{\rho} = (\rho_0, \rho_1, \ldots, \rho_{M-1}, \rho_M)$. (20) is a general solution for the average SEP of an energy detection receiver in a flat fading channel with M-PAM.

3.3.2. Rayleigh fading

Rayleigh distributed path gains are used to model fading channels with no line-of-sight (NLOS) [49, 50, 55]. Thus, the random variable H is *Rayleigh* distributed:

$$f_H(h) = \frac{2h}{\Omega} \exp\left(-\frac{h^2}{\Omega}\right), \quad h \geq 0. \tag{21}$$

In UWB channels with a large bandwidth and a corresponding high temporal resolution, it is questionable, if the central limit theorem is applicable [4, 32, 59]. Nevertheless, some UWB channel measurements show a good fit to the *Rayleigh* distribution [17, 24, 51]. Using (18), the probability density function of the random SNR is:

$$f_\Gamma(\gamma) = \frac{1}{\overline{\gamma}} \exp\left(-\frac{\gamma}{\overline{\gamma}}\right), \quad \gamma \geq 0. \tag{22}$$

Combining (20) and (22) we get an integral of the form:

$$\mathrm{Y}_D(\overline{\gamma}, a_m, \rho_m) = \frac{1}{\overline{\gamma}} \int_0^\infty \mathcal{Q}_D\left(a_m\sqrt{2\gamma}, \sqrt{\rho_m}\right) \exp\left(-\frac{\gamma}{\overline{\gamma}}\right) \mathrm{d}\gamma. \tag{23}$$

The integral in (23) can be solved using [40, eq. 12], given that the interval thresholds do not depend on the instantaneous SNR γ but on the average SNR $\overline{\gamma}$. This is the case for an energy detection receiver with limited channel state information (only knowledge of the average SNR). The closed form solution for Y_D is then:

$$\begin{aligned}\mathrm{Y}_D(\overline{\gamma}, a_m, \rho_m) = \exp\left(-\frac{\rho_m}{2}\right) \Bigg\{ \left(\frac{1/\overline{\gamma} + a_m^2}{a_m^2}\right)^{D-1} \\ \cdot \left[\exp\left(\frac{\rho_m}{2}\frac{a_m^2}{a_m^2 + 1/\overline{\gamma}}\right) - \sum_{d=0}^{D-2} \frac{1}{d!}\left(\frac{\rho_m}{2}\frac{a_m^2}{a_m^2 + 1/\overline{\gamma}}\right)^d\right] + \sum_{d=0}^{D-2} \frac{1}{d!}\left(\frac{\rho_m}{2}\right)^d \Bigg\}.\end{aligned} \tag{24}$$

Combining (20) and (24) yields to the closed form solution for the energy detection receiver in a *Rayleigh* fading channel with M-PAM:

$$\begin{aligned}\overline{P}_{e,ray}(\overline{\gamma}, \mathbf{a}, \boldsymbol{\rho}, M, D) = \frac{1}{M}\Bigg[M - 1 - \mathcal{Q}_D\left(0, \sqrt{\rho_1}\right) \\ + \sum_{m=1}^{M-1} \mathrm{Y}_D\left(\overline{\gamma}, a_m, \rho_m\right) - \sum_{m=1}^{M-2} \mathrm{Y}_D\left(\overline{\gamma}, a_m, \rho_{m+1}\right)\Bigg].\end{aligned} \tag{25}$$

3.3.3. Rician fading

Rice distributed path gains are used to model line-of-sight (LOS) fading channels [49, 50, 55]. Thus, the random variable H is *Rice* distributed:

$$f_H(h) = \frac{2h(k+1)}{\Omega} \exp\left(-k - \frac{(k+1)\,h^2}{\Omega}\right) \mathrm{I}_0\left(2h\sqrt{\frac{k\,(k+1)}{\Omega}}\right), \quad h \geq 0, \tag{26}$$

where I_0 denotes the modified Bessel function of the first kind of order zero. The *Rician*-k-factor is the ratio between the power in the direct path and the power in the scattered paths. For $k = 0$ the *Rice* distribution is equal to the *Rayleigh* distribution. For $k \to \infty$ the *Rician* fading channel converges to the AWGN channel. Different UWB measurement campaigns show a good fit with the distribution of the path gains with a *Rice* distribution [20, 26, 43]. Using (18), the probability density function of the random SNR is:

$$f_\Gamma(\gamma) = \frac{k+1}{\overline{\gamma}} \exp\left(-k - \frac{(k+1)\,\gamma}{\overline{\gamma}}\right) \mathrm{I}_0\left(2\sqrt{\frac{k\,(k+1)\,\gamma}{\overline{\gamma}}}\right), \quad \gamma \geq 0. \tag{27}$$

Combining (20) and (27) we get an integral of the form:

$$\Phi_D(\overline{\gamma}, a_m, \rho_m, k) = \frac{k+1}{\overline{\gamma}} \int_0^\infty \mathcal{Q}_D\left(a_m u, \sqrt{\rho_m}\right) \exp\left(-K - \frac{(K+1)u^2}{\overline{\gamma}}\right) \cdot \mathrm{I}_0\left(2\sqrt{\frac{K\,(K+1)\,u^2}{\overline{\gamma}}}\right) u\,\mathrm{d}u. \tag{28}$$

There exists only a closed form solution for $D = 1$ [39, eq. 45]. In this case, we get:

$$\Phi_1(\overline{\gamma}, a_m, \rho_m, k) = \mathcal{Q}_1\left(\sqrt{\frac{2ka_m^2\gamma}{(k+1)+a_m^2\gamma}}, \sqrt{\frac{(k+1)\rho_m}{(k+1)+a_m^2\gamma}}\right). \tag{29}$$

Thus, the average SEP in a *Rician* fading channel is with a degree of freedom of $2D = 2$:

$$\overline{P}_{e,ric}(\overline{\gamma}, \mathbf{a}, \boldsymbol{\rho}, k, M) = \frac{1}{M}\Bigg[M - 1 - \mathcal{Q}_1\left(0, \sqrt{\rho_1}\right) + \sum_{m=1}^{M-1} \Phi_1\left(\overline{\gamma}, a_m, \rho_m, k\right) - \sum_{m=1}^{M-2} \Phi_1\left(\overline{\gamma}, a_m, \rho_{m+1}, k\right)\Bigg]. \tag{30}$$

A closed form solution for the integral in (28) is not known for $D > 1$. In this case, the integral has to be calculated numerically.

3.3.4. Nakagami-m fading

The probability density function of the *Nakagami-m* distribution of the random path gains is related to the χ^2 distribution:

$$f_H(h) = \frac{2h^{2m-1}}{\Gamma(m)} \left(\frac{m}{\Omega}\right)^m \exp\left(-\frac{m}{\Omega}h^2\right), \quad h \geq 0, \tag{31}$$

where m denotes the *Nakagami-m* fading parameter with $m \in [1/2, \infty)$ and Γ denotes the Gamma function. The *Nakagami-m* distribution includes as special cases the one-sided normal distribution ($m = 1/2$) and the *Rayleigh*-distribution ($m = 1$). For $m \to \infty$ the *Nakagami-m* fading channel converges to the AWGN channel. Different UWB measurement campaigns show a good fit to the *Nakagami-m* distribution [4, 19]. *Nakagami-m* distribution is also used

in the IEEE channel model 802.15.4a to model the path gains [31]. The probability density function of the random SNR Γ is with (18) and (31):

$$f_\Gamma(\gamma) = \frac{\gamma^{m-1}}{\Gamma(m)} \left(\frac{m}{\overline{\gamma}}\right)^m \exp\left(-\frac{m}{\overline{\gamma}}\gamma\right), \quad \gamma \geq 0. \tag{32}$$

In this case we have to solve the following integral by substituting $\gamma = u^2/2$:

$$\int_0^\infty u^{2m-1} \exp\left(-\frac{mu^2}{a\overline{\gamma}}\right) \mathcal{Q}_D\left(au, \sqrt{\rho_m}\right) \mathrm{d}u. \tag{33}$$

(33) can be solved recursively [13]. The average symbol error rate in a fading channel with *Nakagami-m* distributed fading gains is:

$$\begin{aligned}\overline{P}_{e,nak}(\overline{\gamma}, m, \mathbf{a}, \boldsymbol{\rho}, M, D) = \frac{1}{M}\Bigg[& M - 1 - \mathcal{Q}_D\left(0, \sqrt{\rho_1}\right) \\ & + \sum_{\nu=1}^{M-1} \left(A\left(\overline{\gamma}, m, a_\nu, \rho_\nu\right) + \beta_\nu^m B\left(\overline{\gamma}, m, a_\nu, \rho_\nu\right)\right) \\ & - \sum_{\nu=1}^{M-2} \left(A\left(\overline{\gamma}, m, a_\nu, \rho_{\nu-1}\right) + \beta_\nu^m B\left(\overline{\gamma}, m, a_\nu, \rho_{\nu+1}\right)\right)\Bigg],\end{aligned} \tag{34}$$

where

$$A(\overline{\gamma}, m, a, \rho) = \exp\left(-\frac{\beta\rho}{2}\right)\left[\beta^{m-1} L_{m-1}\left(-\frac{(1-\beta)\rho}{2}\right) + (1-\beta)\sum_{i=0}^{m-2} \beta^i L_i\left(-\frac{(1-\beta)\rho}{2}\right)\right]$$

and

$$B(\overline{\gamma}, m, a, \rho) = \exp\left(-\frac{\rho}{2}\right)\sum_{n=1}^{D-1} \frac{\rho_w^n}{2^n n!} {}_1F_1\left(m; n+1; \frac{(1-\beta)\rho}{2}\right) \text{ with } \beta_\nu = \frac{2m}{2m + a_\nu \overline{\gamma}}.$$

L_i is the *Laguerre* polynomial of degree i [18, eq. 8.970] and ${}_1F_1$ is the confluent hypergeometric function [18, eq. 9.210.1].

Figure 12 shows the bit error probability in a flat fading channel with *Rayleigh* and *Rice* distributed channel gains. Figure 13 shows the bit error probability in a flat fading channel with *Nakagami-m* distributed channel gains.

3.4. Diversity reception

Now we analyse the SEP of an energy detection receiver with diversity reception. The goal is to increase the SNR to improve its performance. Because of the architecture of the receiver, detecting only the energy of the received signal, the possibilities to improve its performance are limited and many combining techniques like maximum ratio combining (MRC) or equal gain combining (EGC) are not feasible. Thus we concentrate on square law combining (SLC) and square law selection (SLS) [29].

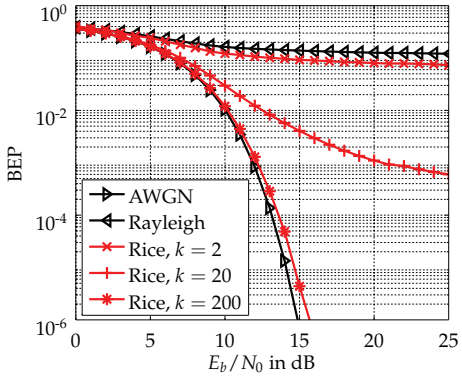

Figure 12. BEP in a flat fading channel with *Rayleigh* and *Rice* distributed channel gains (OOK, $D = 2$)

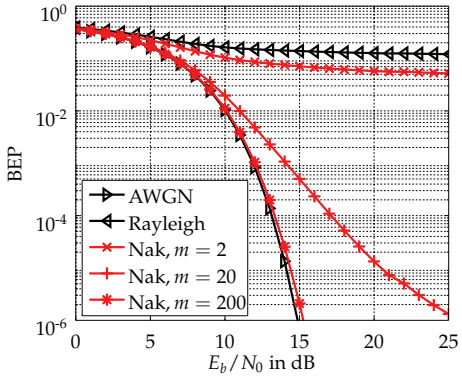

Figure 13. BEP in a flat fading channel with *Nakagami-m* distributed channel gains (OOK, $D = 2$)

The channel model used here is based on flat fading with independent and correlated fading gains H_l for all l diversity paths. The instantaneous SNR at the energy detector l is:

$$\gamma_l = h_l^2 E_S / N_{0,l}$$

and the average SNR at the l^{th} detector is:

$$\overline{\gamma}_l = \Omega_l E_S / N_{0,l}$$

with $\Omega_l = \mathbb{E}(H_l^2)$. Figure 14 shows the model of multichannel receiver.

3.4.1. Square law combining

At the SLC receiver we have a new SNR Y_{SLC} at the receiver output based on the sum of the SNR Y_l at the l detectors:

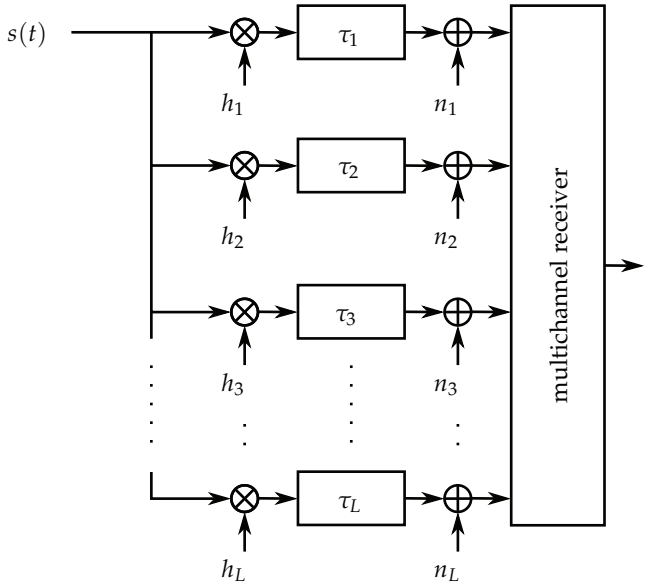

Figure 14. Channel model for multichannel receiver

$$Y_{\mathrm{SLC}} = \sum_{l=1}^{L} Y_l.$$

The new random variable Y_{SLC} has a central χ^2 distribution for $a_0 = 0$ and a noncentral χ^2 distribution for $a_m > 0$ with the degree of freedom of $2LD$. The conditional distribution function for SLC is:

$$F_{Y|A}(y|a_m) = \mathcal{Q}_{LD}(a_m\sqrt{\gamma_{\mathrm{SLC}}}, \sqrt{y}) \tag{35}$$

with the non centrality parameter:

$$\mu_{\mathrm{SLC}} = 2\gamma_{\mathrm{SLC}} = 2\sum_{l=1}^{L}\gamma_l.$$

Thus the SEP in L parallel AWGN channels with different SNR γ_l using SLC is:

$$P_e(\gamma_{\mathrm{SLC}}, \mathbf{a}, \tilde{\boldsymbol{\rho}}, M, D, L) = \frac{1}{M}\left[M - 1 + \sum_{m=1}^{M-1}\mathcal{Q}_{LD}\left(\sqrt{a_m^2\gamma_{\mathrm{SLC}}}, \sqrt{\tilde{\rho}_m}\right)\right.$$
$$\left. - \sum_{m=0}^{M-2}\mathcal{Q}_{LD}\left(\sqrt{a_m^2\gamma_{\mathrm{SLC}}}, \sqrt{\tilde{\rho}_{m+1}}\right)\right],$$

where $\tilde{\rho}$ are the optimal interval thresholds (section 3.2.1.1), based on the new random variable Y_{SLC}.

3.4.1.1. Independent and identically distributed Rayleigh distributed channel gains

Now we derive the SEP for SLC with independent and identical distributed (i.i.d.) Rayleigh distributed channel gains H_l. The SNR Γ_l is exponential distributed for all l. The probability density function $f_{\Gamma_{\mathrm{SLC}}}$ of $\Gamma_{\mathrm{SLC}} = \sum_{l=1}^{L} \Gamma_l$ with $\overline{\gamma} = \mathbb{E}(\Gamma_l)$ is [27, eq. 10.61]:

$$f_{\Gamma_{\mathrm{SLC}}}(\gamma_{\mathrm{SLC}}) = \frac{\gamma_{\mathrm{SLC}}^{L-1}}{(L-1)!\overline{\gamma}^{L}} \exp\left(\frac{\gamma_{\mathrm{SLC}}}{\overline{\gamma}}\right). \tag{36}$$

Comparing (36) with the probability density function of the SNR with *Nakagami-m* distributed channel gains we get the average SEP in I.I.D. *Rayleigh* fading channels:

$$\overline{P}_{e,SLC}(\overline{\gamma}, \mathbf{a}, \tilde{\boldsymbol{\rho}}, M, D, L) = \overline{P}_{e,nak}(L\overline{\gamma}, L, \mathbf{a}, \tilde{\boldsymbol{\rho}}, M, LD),$$

substituting $\overline{\gamma}$ by $L\overline{\gamma}$, m by L, $\boldsymbol{\rho}$ by $\tilde{\boldsymbol{\rho}}$ and $2D$ by $2LD$. The intervall thresholds $\tilde{\boldsymbol{\rho}}$ are based on $L\overline{\gamma}$.

3.4.1.2. Correlated Rayleigh distributed channel gains

In the next step, we assume correlated *Rayleigh* distributed channel gains H_l. In this case the probability density function of the SNR Γ is a sum of weighted exponential distributions [27, eq. 10.60]:

$$f_{\Gamma_{\mathrm{SLC}}}(\gamma_{\mathrm{SLC}}) = c_1 \sum_{l=1}^{L} c_{2,l} \exp\left(\frac{\gamma_{\mathrm{SLC}}}{\overline{\gamma}}\right) \tag{37}$$

with

$$c_1 = \frac{1}{\Pi_{l=1}^{L}\lambda_l}, \quad c_{2,l} = \frac{1}{\Pi_{l\neq k}^{L}(1/\lambda_k - 1/\lambda_l)},$$

where λ_l are the eigenvalues of the $L \times L$ covariance matrix $\boldsymbol{\Sigma}$ of the normalized received signal. Using the function Y (24) the SEP in a fading channel with correlated *Rayleigh* distributed fading gains can be written as:

$$\begin{aligned}\overline{P}_{e,\mathrm{SLC}}(\overline{\gamma}, \mathbf{a}, \tilde{\boldsymbol{\rho}}, M, D, L) = \frac{1}{M}\Bigg[& M - 1 - \mathcal{Q}_{LD}\left(0, \sqrt{\rho_1}\right) \\ & + c_1 \sum_{m=1}^{M-1}\sum_{l=1}^{L} \lambda_l c_{2,l} \mathrm{Y}_{LD}\left(\lambda_l, a_m, \tilde{\rho}_m\right) \\ & - c_1 \sum_{m=1}^{M-2}\sum_{l=1}^{L} \lambda_l c_{2,l} \mathrm{Y}_{LD}\left(\lambda_l, a_m, \tilde{\rho}_{m+1}\right)\Bigg].\end{aligned}$$

3.4.2. Square law selection

The receiver based on SLS chooses the detector with the highest received energy $Y_{\max}$:

$$Y_{\max} = \max(Y_1, Y_2, \ldots, Y_L). \tag{38}$$

Thus, this receiver collects only a fraction of the total received energy. Using (9) and (38), the SEP with SLS in the AWGN channel is:

$$\begin{aligned} P_e(\gamma, \mathbf{a}, \boldsymbol{\rho}, D, L) &= 1 - P_c(\gamma, \mathbf{a}, \boldsymbol{\rho}, D) \\ &= 1 - \sum_{m=0}^{M-1} \mathbb{P}(\rho_m < Y_{\max} \leq \rho_{m+1} | A = a_m) \mathbb{P}(A = a_m). \end{aligned} \tag{39}$$

In order to calculate (39), we calculate the probability that $Y_{\max}$ is in the interval $(\rho_m, \rho_{m+1}]$:

$$\begin{aligned} &\mathbb{P}(\rho_m < Y_{\max} \leq \rho_{m+1} | A = a_m) \\ &= \mathbb{P}\left(\bigcap_{l=1}^{L} \{Y_l < \rho_{m+1} | A = a_m\} \right) - \mathbb{P}\left(\bigcap_{l=1}^{L} \{Y_l < \rho_m | A = a_m\} \right). \end{aligned} \tag{40}$$

If all received energies Y_l are independent, (40) reduces to:

$$\mathbb{P}\left(\bigcap_{l=1}^{L} \{Y_l < \rho_m | A = a_m\} \right) = \prod_{l=1}^{L} \mathbb{P}\left(Y_l < \rho_m | \, A = a_m\right). \tag{41}$$

Using the distribution function (14), the probability can be written as:

$$\mathbb{P}\left(Y_l < \rho_m | \, A = a_m\right) = 1 - Q_D\left(a_m \sqrt{\gamma}, \sqrt{\rho_m}\right). \tag{42}$$

Combining (40), (41) and (42) and assume $\mathbb{P}(A = a_m) = 1/M$, (39) can be written as:

$$\begin{aligned} P_e(\gamma, \mathbf{a}, \boldsymbol{\rho}, D, L) = 1 - \frac{1}{M} \sum_{m=0}^{M-1} \Bigg[&\prod_{l=1}^{L} \left(1 - Q_D\left(a_m \sqrt{\gamma_l}, \sqrt{\rho_{m+1,l}}\right)\right) \\ &- \prod_{l=1}^{L} \left(1 - Q_D\left(a_m \sqrt{\gamma_l}, \sqrt{\rho_{m,l}}\right)\right) \Bigg], \end{aligned} \tag{43}$$

where $\rho_{m,l}$ denotes the optimal interval thresholds which are based on the SNR γ_l. If all received energies Y_l are independent and identical distributed, (41) reduces to:

$$\prod_{l=1}^{L} \mathbb{P}\left(Y_l < \rho_m | A = a_m\right) = \left(1 - Q_D\left(a_m \sqrt{\gamma}, \sqrt{\rho_m}\right)\right)^L. \tag{44}$$

In this case, (43) reduces to:

$$\begin{aligned} P_e(\gamma, \mathbf{a}, \boldsymbol{\rho}, D, L) = 1 - \frac{1}{M} \sum_{m=0}^{M-1} \Big[&\left(1 - Q_D\left(a_m \sqrt{\gamma}, \sqrt{\rho_{m+1}}\right)\right)^L \\ &- \left(1 - Q_D\left(a_m \sqrt{\gamma}, \sqrt{\rho_m}\right)\right)^L \Big]. \end{aligned}$$

If the SNR is independent and identically *Rayleigh* distributed with $\overline{\gamma} = \mathbb{E}(\Gamma_l)$ for all l, the SEP in a fading channel with i.i.d. *Rayleigh* distributed channel gains can be written using the

function Y (24):

$$P_e(\overline{\gamma}, \mathbf{a}, \boldsymbol{\rho}, D, L) = \frac{1}{M}\Bigg[M + 1 + \left(1 - Q_D\left(a_0\sqrt{\overline{\gamma}}, \sqrt{\rho_1}\right)\right)^L + \sum_{m=1}^{M-2}\left(1 - \mathrm{Y}_D(\overline{\gamma}, a_m, \rho_{m+1})\right)^L - \sum_{m=1}^{M-1}\left(1 - \mathrm{Y}_D(\overline{\gamma}, a_m, \rho_m)\right)^L\Bigg].$$

Figure 15 shows the gain that can be achieved using SLC. Figure 16 shows the gain that can be achieved using SLS. The SLC based receiver can collect more energy, but also more noise than the SLS based receiver. The SLS based receiver chooses only the dominant path.

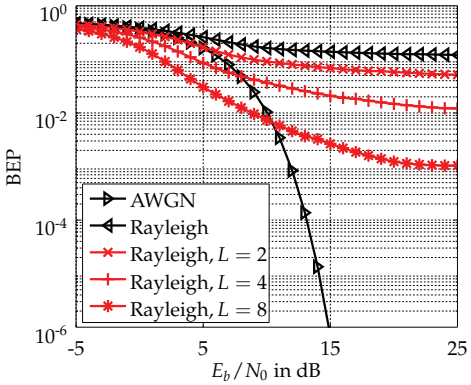

Figure 15. BEP in the *Rayleigh* channel with SLC

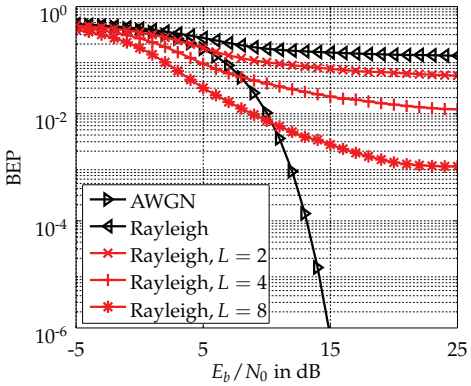

Figure 16. BEP in the *Rayleigh* channel with SLS

3.5. Frequency selective fading channel

Now we focus on the frequency selectivity of a channel and the effect on the SEP for an energy detection receiver. The received signal $\boldsymbol{R}$ is in the baseband equivalent model:

$$\boldsymbol{R} = \underbrace{\boldsymbol{x}\boldsymbol{H}}_{\boldsymbol{S}} + \boldsymbol{W},$$

where $\boldsymbol{H} = (H_1, \ldots, H_L)^T$ denotes the random channel impulse response, circular symmetric complex white Gaussian noise $\boldsymbol{W} \sim \mathcal{CN}_L\left(\mathbf{0}, \sigma_n^2\mathbf{I}\right)$ and $\boldsymbol{x}$ denotes the convolution matrix, containing shifted versions of the transmitted signal:

$$\mathbf{x} = \begin{pmatrix} s_1 & 0 & \ldots & 0 \\ s_2 & s_1 & \ldots & 0 \\ \vdots & \vdots & \ddots & \vdots \\ s_L & s_{L-1} & \ldots & s_1 \end{pmatrix}.$$

The effect of intersymbol interference has not been taken into account by choosing a gap between symbols larger than the channel delay spread. Using the quadratic form of $\boldsymbol{S}$ the SNR Γ at the receiver can be written as:

$$\Gamma = \frac{E_R}{N_0} = \frac{\boldsymbol{S}^H\boldsymbol{S}}{4N_0B}.$$

3.5.1. NLOS fading channel

In an environment with no line of sight between transmitter and receiver, the expectation of the random samples of the channel impulse response $\boldsymbol{H}$ is zero:

$$\boldsymbol{H} \sim \mathcal{CN}_D\left(\mathbf{0}, \mathbf{\Sigma}\right) \quad \text{with } \mathbf{\Sigma}(i,j) = h_i h_j e^{-\frac{|i-j|}{\beta}},$$

where $\beta > 0$ describes the correlation of the elements in the covariance matrix $\mathbf{\Sigma}$. If the samples of the channel impulse response are uncorrelated, $\mathbf{\Sigma}$ is a diagonal matrix. The expectation the noise free received signal is also zero:

$$\boldsymbol{S} = \boldsymbol{x}\boldsymbol{H} \sim \mathcal{CN}_D\left(\mathbf{0}, \mathbf{\Sigma}_s\right) \quad \text{with } \mathbf{\Sigma}_s = \boldsymbol{x}\mathbf{\Sigma}\boldsymbol{x}^H.$$

Let $\mathbf{\Sigma}_s^{\frac{1}{2}}$ denote a matrix that fulfils $\mathbf{\Sigma}_s^{\frac{1}{2}}\mathbf{\Sigma}_s^{\frac{1}{2}} = \mathbf{\Sigma}_s$, then a whitened vector $\mathbf{S}' \sim \mathcal{CN}_L\left(\mathbf{0}, \mathbf{I}\right)$ is defined as

$$\mathbf{\Sigma}_s^{-\frac{1}{2}}\mathbf{S} = \mathbf{S}'. \tag{45}$$

Note that the existence of $\mathbf{\Sigma}_s^{\frac{1}{2}}$ is guaranteed for any positive definite matrix $\mathbf{\Sigma}_s$. To calculate the distribution of instantaneous SNR Γ, we need to analyse the distribution of $\mathbf{S}^H\mathbf{S}$ first. Using (45) yields

$$\mathbf{S}^H\mathbf{S} = \mathbf{S}'^H\mathbf{\Sigma}_s\mathbf{S}'. \tag{46}$$

Using eigenvalue decomposition and special properties of the central χ^2-distribution, a closed form expression for the PDF of $\mathbf{r}^H\mathbf{r}$ can be found [21]. Performing an eigenvalue

decomposition of $\mathbf{\Sigma}_S$ in (46) leads to

$$\mathbf{S}^H\mathbf{S} = \mathbf{S}'^H\mathbf{U}^H\mathbf{\Lambda}\mathbf{U}\mathbf{S}'$$

with $\mathbf{\Lambda}$ being a diagonal matrix containing the eigenvalues $\lambda_1, \ldots, \lambda_L$ of $\mathbf{\Sigma}_s$ and the rows of unitary matrix $\mathbf{U}$ being the corresponding eigenvectors. Substituting $\mathbf{G} = \mathbf{U}\mathbf{S}'$, the random variable V is:

$$V = \mathbf{S}^H\mathbf{S} = \mathbf{G}^H\mathbf{\Lambda}\mathbf{G} = \sum_{l=1}^{L} \lambda_l G_l G_l^* \tag{47}$$

with G_l representing the elements of $\mathbf{G}$ and G_l^* denoting the complex conjugate of G_l. Note that $\mathbf{G}$ and $\mathbf{H}$ are equally distributed because the rows of $\mathbf{U}$ are orthonormal among each other. Therefore

$$\mathbf{G} \sim \mathcal{CN}_L\left(\mathbf{0}, \mathbf{\Sigma}_s\right).$$

The random variable $G_l' = G_l G_l^* = |G_l|^2$ is central χ^2 distributed with two degrees of freedom. That is a special case of the central χ^2 distribution which is equivalent to an exponential distribution. As a linear combination of independent and identically exponential distributed variates, V is general *Gamma* or general *Erlang* distributed with the PDF given as [21, eq. 19.147]:

$$f_V(v) = \sum_{j=1}^{D} \left(\prod_{k \neq j} \left(\lambda_j - \lambda_k\right)^{-1} \right) \lambda_j^{D-2} e^{-\frac{v}{\lambda_j}}. \tag{48}$$

The average SNR $\overline{\gamma}$ is based on the expectation of the random variable V:

$$\overline{\gamma} = \frac{\mathbb{E}(V)}{4N_0B}. \tag{49}$$

Because all random variables G_i are independent $\mathbb{E}(V)$ can be written as:

$$\mathbb{E}(V) = \sum_{i=1}^{D} \lambda_i \mathbb{E}(|G_i|^2) = 2\sum_{i=1}^{D} \lambda_i \quad \text{with } \mathbb{E}(|G_i|^2) = 2.$$

Introducing a change of variable in (48) yields:

$$f_\Gamma(\gamma) = 2N_0B\, f_V\left(2N_0B\gamma\right). \tag{50}$$

Using the relative SNR $\gamma' = \frac{\gamma}{\overline{\gamma}}$, (50) can be expressed as:

$$f_{\Gamma'}\left(\gamma'\right) = 2N_0B\overline{\gamma}\, f_V\left(2N_0B\overline{\gamma}\gamma'\right). \tag{51}$$

The SEP in a fading channel can be calculated using (20). Combining (20) and (51) yields to the following integral:

$$2N_0B \sum_{j=1}^{D} \left(\prod_{k \neq j} \left(\lambda_j - \lambda_k\right)^{-1} \right) \lambda_j^{D-2} \int_0^\infty \mathcal{Q}_D\left(\sqrt{a_m^2\overline{\gamma}\gamma'}, \sqrt{\rho_m}\right) e^{-\frac{2N_0B}{b\lambda_j}\overline{\gamma}\gamma'}\, \mathrm{d}\gamma'.$$

In the case of partial CSI, the integral can be solved using [40, eq. 12] with adequate substitutions:

$$\Theta_D(\overline{\gamma}, N_0, \boldsymbol{\lambda}, B, a_m, \rho_m) = \frac{1}{\overline{\gamma}} \sum_{j=1}^{D} \left(\prod_{k \neq j} \left(\lambda_j - \lambda_k \right)^{-1} \right) \lambda_j^{D-2} \mathrm{e}^{-\frac{\rho_m}{2}} \left\{ \left(1 + \frac{2N_0 B}{a_m^2 \lambda_j} \right)^{D-1} \cdot \left[\exp\left(\frac{\rho_m}{2} \frac{1}{1 + \frac{2N_0 B}{a_m^2 \lambda_j}} \right) - \sum_{n=0}^{D-2} \frac{1}{n!} \left(\frac{\rho_m}{2} \frac{1}{1 + \frac{2N_0 B}{a_m^2 \lambda_j}} \right)^n \right] + \sum_{n=0}^{D-2} \frac{1}{n!} \left(\frac{\rho_m}{2} \right)^n \right\}. \quad (52)$$

Using the function Θ_D (52), the average SEP in a frequency selective fading channel can be expressed in closed form [3]:

$$\overline{P}_e(\overline{\gamma}, N_0, B, \boldsymbol{a}, \boldsymbol{\rho}, \boldsymbol{\lambda}, M, D) = \frac{1}{M} \Bigg[M - 1 + \mathcal{Q}_D\left(0, \sqrt{\rho_1}\right) + \sum_{m=1}^{M-1} \Theta_D(\overline{\gamma}, N_0, \boldsymbol{\lambda}, B, a_m, \rho_m) - \sum_{m=1}^{M-2} \Theta_D(\overline{\gamma}, N_0, \boldsymbol{\lambda}, B, a_m, \rho_{m+1}) \Bigg].$$

This equation is only valid if two constraints are met:

1. The receiver may only use $\overline{\rho}$ to determine the decision threshold (partial CSI) and
2. all eigenvalues λ_j are pairwise disjunct.

If there exist two or more identical eigenvalues, one might rearrange (47) and decrease D used in the subsequent calculations to meet the second constraint. Figure 17 shows the BEP in the frequency selective fading channel with i.i.d. and correlated channel gains.

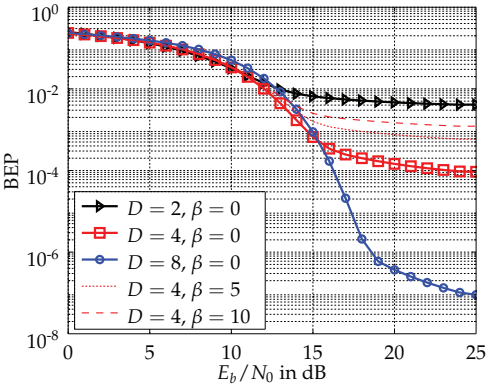

Figure 17. BEP for OOK in the frequency selective fading channel

3.5.2. LOS fading channel

In a channel model with LOS, $\mathbf{H}$ is expected to have a non-zero mean vector $\mathbf{M}$. Therefore V is equal in distribution to a linear combination of noncentral χ^2 distributed variates. Unfortunately, there is no such convenient correspondence for that distribution as the general *Erlang* distribution for V in section 3.5.1.

Even though the PDF of a linear combination of noncentral χ^2 distributed variates is given in [48], there is no known closed-form expression for the integral of the product of this PDF and the MARCUM-Q-function in (20).

The average SEP may still be computed using a discrete approximation of the PDF of V (histogram). This histogram can be generated with arbitrary precision by sampling the PDF given in [48] or by performing a Monte-Carlo-simulation based on the distribution of $\mathbf{H}$. For the Monte-Carlo-simulations the samples of the LOS channel impulse response $\mathbf{H}$ follow a normal distribution

$$\mathbf{H} \sim \mathcal{CN}_L\left(\mathbf{M}, \mathbf{\Sigma_h}\right)$$

with the mean $\mathbf{M} = (M_1, \ldots, M_D)$ with $M_i = \sqrt{\frac{\kappa}{\kappa+1}}\ \forall\ i$ and the covariance matrix $\mathbf{\Sigma_h} = \frac{1}{\kappa+1}\mathbf{I}$.

4. Interference investigations for non-coherent multiband UWB

As the unlicensed MIR-UWB system has no exclusive frequency range there is an increased interference potential from present and from future radio systems operating in the same frequency range. Hence, the performance of the MIR-UWB system can be reduced and a reliable communication cannot be guaranteed at any time. For this reason it is imperative to realise an efficient and low complex interference mitigation.

Section 4 is structured as follows: In section 4.1 an analysis of the interference robustness of an energy detection receiver is presented. This allows the identification of suitable MIR-UWB system parameters which can be configured preferably robust against interferences before initial operation of the MIR-UWB system. The following section 4.2 deals with coexistence-based approaches which are focused on an efficient and adaptive interference mitigation with low complexity. As the mitigation of narrowband interference (NBI) is a crucial issue of the MIR-UWB section 4.3 analyses the non-linear Teager-Kaiser (TK) operation. Thereby, the potential to mitigate NBI and to integrate the TK operation into the existing MIR UWB system is shown.

4.1. Interference robustness of energy detection

A basic issue of the MIR-UWB's energy detection receiver is its high sensitivity with respect to interferences passing the analogue front-end. A significant reduction of the instantaneous Signal-to-Interference-and Noise Ratio (SINR) can occur so that a reliable communication is not guaranteed.

For this reason it is required to investigate the interference robustness of an OOK and BPPM specific energy detection [7, 9]. The analysis bases on an analytical investigation of the interference robustness of an energy detector within an arbitrary but fixed subband. Thereby, dependencies between system- and interference specific parameters can be identified which

promise an increase of interference robustness. The analysis bases on one hand on [53]. Therein, the performance of a BPPM specific energy detector is analysed in presence of out-of-band interference. On the other hand it relies on [60] in which the performance of a BPPM specific correlation receiver is investigated in presence of interference.

4.1.1. Signal model

Binary data transmission within an MIR-UWB subband of bandwidth B is considered. Thereby, based on OOK/BPPM the rectangular pulse

$$p(t) = \begin{cases} \sqrt{\frac{2}{T_\mathrm{p}}} \cos(2\pi f_\mathrm{c} t) & ,0 < t < T_\mathrm{p} \\ 0 & ,\text{else} \end{cases} \tag{53}$$

with carrier frequency f_c and pulse duration T_p is emitted with energy 1 ($f_\mathrm{c} \gg 1/T_\mathrm{p}$). The resulting signal to be transmitted conducts to

$$s_\mathrm{O}(t) = \sqrt{E_\mathrm{p}^\mathrm{O}} \sum_{n=-\infty}^{\infty} b_n p_i(t - nT_\mathrm{b}) \tag{54}$$

for OOK and

$$s_\mathrm{P}(t) = \sqrt{E_\mathrm{p}^\mathrm{P}} \sum_{n=-\infty}^{\infty} p_i\left(t - nT_\mathrm{b} - b_n \frac{T_\mathrm{b}}{2}\right) \tag{55}$$

for BPPM. The uniformly distributed data bit $b_n \in \{0,1\}$ is characterised by bit energy E_b as well as by bit duration $T_\mathrm{b} = \frac{T_\mathrm{p}}{d_\mathrm{s}}, d_\mathrm{s} > 0$ with duty cycle $d_\mathrm{s} \leq \frac{1}{2}$. Finally, $E_\mathrm{p}^i, i \in \{\mathrm{O}, \mathrm{P}\}$ stands for the modulation specific pulse energy which equals $E_\mathrm{p}^\mathrm{O} = 2E_\mathrm{p}^\mathrm{P} = 2E_\mathrm{b}$.

Assuming perfect synchronisation between the transmitter and the receiver, the signal $s_i(t), i \in \{\mathrm{O}, \mathrm{P}\}$ is superposed with zero mean white Gaussian noise $n(t)$ of two-sided spectral density $\frac{N_0}{2}$ and interference $j(t)$ leading to (no fading)

$$y_i(t) = s_i(t) + n(t) + j(t). \tag{56}$$

Interference is described as band-limited wide-sense stationary, time-continuous zero mean Gaussian process $J(t)$ characterised by the autocorrelation function ($\tau = t_1 - t_2$)

$$R_\mathrm{J}(\tau) = P_\mathrm{J} \frac{\sin(\pi B_\mathrm{J} \tau)}{\pi B_\mathrm{J} \tau} \cos(2\pi f_\mathrm{J} \tau). \tag{57}$$

It depends on the mean interference power P_J determined by the ratio of the interferer's bit energy $E_\mathrm{b,J}$ and bit duration $T_\mathrm{b,J} = qT_\mathrm{b}, q > 0$. Further parameters are the interference center frequency f_J as well as its bandwidth B_J.[1] The resulting interferer's signal duration $T_\mathrm{p,J} \approx \frac{1}{B_\mathrm{J}} \leq T_\mathrm{b,J}$ leads to an interference duty cycle of $d_\mathrm{J} = \frac{T_\mathrm{p,J}}{T_\mathrm{b,J}} = \frac{d_\mathrm{s} T_\mathrm{p,J}}{qT_\mathrm{p}}$.

[1] Eq. (57) holds if the interference source is completely inside the MIR-UWB subband. In case B_J overlaps completely or only partially with the subband f_J, B_J and P_J have to be properly modified. However, as it can be ascribed to (57) the following investigations focus solely on an interference source being completely inside the subband.

The received signal of (56) is first bandpass filtered and afterwards subjected to non-coherent energy detection with integration time T_p. At its input stage the available SINR is given by

$$\mathrm{SINR_E} = 10\log_{10}\frac{E_\mathrm{b}}{T_\mathrm{b}\left(P_\mathrm{J}+P_\mathrm{N}\right)}, \tag{58}$$

which is identical for OOK/BPPM. In (58) P_N stands for the mean noise power of the passband noise signal, which is modelled as band-limited wide-sense stationary, time-continuous zero mean Gaussian process $N(t)$: $(\tau = t_1 - t_2)$

$$R_\mathrm{N}(\tau) = P_\mathrm{N}\frac{\sin(\pi B\tau)}{\pi B\tau}\cos(2\pi f_\mathrm{c}\tau). \tag{59}$$

At the output of energy detection the decision variable differs for OOK/BPPM.

Energy detection of OOK
For OOK, the asymmetric decision variable

$$x^\mathrm{O} = \int_0^{T_\mathrm{p}} y^2(t)\,\mathrm{d}t = x_\mathrm{s}^\mathrm{O} + \Delta x^\mathrm{O} \tag{60}$$

occurs. The resulting energy value x^O consists of a deterministic signal-only part

$$x_\mathrm{s}^\mathrm{O} = \begin{cases} 0 & ,b_n = 0 \\ 2E_\mathrm{b} & ,b_n = 1 \end{cases} \tag{61}$$

of mean E_b and second order moment $2E_\mathrm{b}^2$. The component $\Delta x^\mathrm{O} = x_\mathrm{sjn}^\mathrm{O} + x_\mathrm{jn}^\mathrm{O}$ contains the mixed signal-noise and signal-interference term

$$x_\mathrm{sjn}^\mathrm{O} = \begin{cases} 0 & ,b_n = 0 \\ 2\sqrt{\frac{2E_\mathrm{p}^\mathrm{O}}{T_\mathrm{p}}}\int_0^{T_\mathrm{p}}\cos(2\pi f_\mathrm{c}t)\left(n(t)+j(t)\right)\mathrm{d}t\mathrm{d}t & ,b_n = 1 \end{cases} \tag{62}$$

as well as the contribution

$$x_\mathrm{jn}^\mathrm{O} = \int_0^{T_\mathrm{p}}\left(n(t)+j(t)\right)^2\mathrm{d}t \quad ,b_n = 0,1 \tag{63}$$

due to noise and interference-only.

Energy detection of BPPM
In contrast to OOK the BPPM specific decision variable at the output of energy detection is symmetric:

$$x^\mathrm{P} = \int_0^{T_\mathrm{p}} y_\mathrm{P}^2(t)\,\mathrm{d}t - \int_{\frac{T_\mathrm{b}}{2}}^{\frac{T_\mathrm{b}}{2}+T_\mathrm{p}} y_\mathrm{P}^2(t)\,\mathrm{d}t = x_\mathrm{s}^\mathrm{P} + \Delta x^\mathrm{P}. \tag{64}$$

The decision variable x^{P} compares energy values within two observation intervals of duration T_{p}. [2] It is composed of a signal-only contribution

$$x_s^{\mathrm{P}} = \begin{cases} E_{\mathrm{b}} & , b_n = 0 \\ -E_{\mathrm{b}} & , b_n = 1, \end{cases} \tag{65}$$

which is characterised by mean zero and second order moment E_{b}^2. The additional term $\Delta x^{\mathrm{P}} = x_{\mathrm{sjn}}^{\mathrm{P}} + x_{\mathrm{jn}}^{\mathrm{P}}$ is on one hand composed of a mixed signal-noise and signal-interference component

$$x_{\mathrm{sjn}}^{\mathrm{P}} = \begin{cases} a \int\limits_0^{T_{\mathrm{p}}} \cos\left(2\pi f_{\mathrm{c}} t\right) \left(n\left(t\right) + j\left(t\right)\right) \mathrm{d}t & , b_n = 0 \\ -a \int\limits_{\frac{T_{\mathrm{b}}}{2}}^{\frac{T_{\mathrm{b}}}{2}+T_{\mathrm{p}}} \cos\left(2\pi f_{\mathrm{c}} \left(t - \frac{T_{\mathrm{b}}}{2}\right)\right) \left(n\left(t\right) + j\left(t\right)\right) \mathrm{d}t & , b_n = 1 \end{cases} \tag{66}$$

with $a = 2\sqrt{2E_{\mathrm{P}}^{\mathrm{P}} / T_{\mathrm{p}}}$. On the other hand it consists of the noise and interference-only part

$$x_{\mathrm{jn}}^{\mathrm{P}} = \int\limits_0^{T_{\mathrm{p}}} \left(n\left(t\right) + j\left(t\right)\right)^2 \mathrm{d}t - \int\limits_{\frac{T_{\mathrm{b}}}{2}}^{\frac{T_{\mathrm{b}}}{2}+T_{\mathrm{p}}} \left(n\left(t\right) + j\left(t\right)\right)^2 \mathrm{d}t. \tag{67}$$

4.1.2. Statistical analysis of interference robustness

To make statements on the interference robustness of an OOK and BPPM specific energy detection a proper quality criterion has to be introduced. A possible measure is the processing gain (PG) of the energy detector. It refers the available SINR at its output to the $\mathrm{SINR_E}$ at its input. For OOK this can be described as

$$\mathrm{PG}^{\mathrm{O}} = 10\log_{10}\left(\frac{2E_{\mathrm{b}}^2}{0,5Q_1^{\mathrm{O}} + Q_2^{\mathrm{O}}}\right) - 10\log_{10}\left(\mathrm{SINR_E}\right), \tag{68}$$

which differs from the PG of the BPPM based energy detection receiver expressed as

$$\mathrm{PG}^{\mathrm{P}} = 10\log_{10}\left(\frac{E_{\mathrm{b}}^2}{Q_1^{\mathrm{P}} + Q_2^{\mathrm{P}}}\right) - 10\log_{10}\left(\mathrm{SINR_E}\right). \tag{69}$$

In (68) and (69) $Q_1^i, i \in \{\mathrm{O}, \mathrm{P}\}$ stands for the second order moment of the mixed signal-noise and signal-interference component $x_{\mathrm{sjn}}^i, i \in \{\mathrm{O}, \mathrm{P}\}$. In contrast, $Q_2^i, i \in \{\mathrm{O}, \mathrm{P}\}$ describes the second order moment of the noise and interference-only part $x_{\mathrm{jn}}^i, i \in \{\mathrm{O}, \mathrm{P}\}$.

Based on PG, separate statements on the detection performance can be made for each modulation scheme, i.e., a low modulation specific PG indicates an increased error probability

[2] It is assumed that the pulse of duration $T_{\mathrm{p}} \leq \frac{T_{\mathrm{b}}}{2}$ occurs at the beginning of an interval of duration $\frac{T_{\mathrm{b}}}{2}$. Hence, the position of a pulse within the interval is perfectly known.

and vice versa. Hence, the smaller Q_1^i and $Q_2^i, i \in \{\mathrm{O}, \mathrm{P}\}$ the lower the modulation related error detection probability. In the following, Q_1^i and $Q_2^i, i \in \{\mathrm{O}, \mathrm{P}\}$ are determined for both modulation schemes.

OOK: For OOK the second order moment of the signal-noise and signal-interference part $x_{\mathrm{sjn}}^{\mathrm{O}}$ can be formulated as ($\tau = t_1 - t_2$)

$$Q_1^{\mathrm{O}} = \int_{-t_1}^{T_\mathrm{P}-t_1} \int_{0}^{T_\mathrm{P}} \left(R_\mathrm{J}(\tau) + R_\mathrm{N}(\tau)\right) \cdot p(t_1) \cdot p(t_1+\tau)\, \mathrm{d}t_1 \mathrm{d}\tau. \tag{70}$$

A general solution of Q_1^{O} can be found using Parseval's theorem under the assumptions $2|f_\mathrm{c} + f_\mathrm{J}| \gg B_\mathrm{J}$ and $4f_\mathrm{c} \gg B$. This leads to the closed-form expression

$$\begin{aligned} Q_1^{\mathrm{O}} = {} & E_\mathrm{p}^{\mathrm{O}} P_\mathrm{J} \sum_{n=0}^{\infty} (-1)^n \left(2\pi T_\mathrm{p}\right)^{2n} \left(\frac{r_{2n+1} \sum_{l=0}^{2n+1} u_{n,l}}{2\pi f_\mathrm{c}\,(2n+1)} \right. \\ & \left. - \frac{2\pi T_\mathrm{p} r_{2n+2} \sum_{l=0}^{2n+2} v_{n,l}}{2\pi f_\mathrm{c}\,(2n+2)} + \frac{4T_\mathrm{p} r_{2n+1}}{(2n+2)!\,(2n+1)} \right) \\ & + \frac{E_\mathrm{p}^{\mathrm{O}} P_\mathrm{N}}{2\pi f_\mathrm{c}} \sum_{n=0}^{\infty} \frac{(-1)^n \left(\pi T_\mathrm{p} B_\mathrm{T}\right)^{2n}}{(2n+1)} \left(\frac{8\pi T_\mathrm{p} f_\mathrm{c}}{(2n+2)!} + (1+ \right. \\ & \left. \cos\left(4\pi f_\mathrm{c} T_\mathrm{p}\right)) \sum_{l=0}^{2n+1} w_{n,l} - \sin\left(4\pi f_\mathrm{c} T_\mathrm{p}\right) \sum_{l=0}^{2n+1} z_{n,l} \right), \end{aligned} \tag{71}$$

whereas, with $\Delta_{f_{\mathrm{c,J}}} = f_\mathrm{c} - f_\mathrm{J}$, the following notations are used:

$$\begin{aligned} r_\nu &= \frac{1}{B_\mathrm{J}} \left(\left(\frac{B_\mathrm{J}}{2} + \Delta_{f_{\mathrm{c,J}}} \right)^\nu - \left(-\frac{B_\mathrm{J}}{2} + \Delta_{f_{\mathrm{c,J}}} \right)^\nu \right), \\ w_{n,l} &= \frac{\sin\left(4\pi f_\mathrm{c} T_\mathrm{p} + \frac{1}{2} l\pi\right)}{(2n+1-l)!\left(4\pi f_\mathrm{c} T_\mathrm{p}\right)^l}, \\ u_{n,l} &= w_{n,l} + \frac{(-1)^l}{(2n+1-l)!} \sum_{k=0}^{l} \frac{\sin\left(4\pi f_\mathrm{c} T_\mathrm{p} + \frac{1}{2} k\pi\right)}{(l-k)!\left(4\pi f_\mathrm{c} T_\mathrm{p}\right)^k}, \\ z_{n,l} &= \frac{\cos\left(4\pi f_\mathrm{c} T_\mathrm{p} + \frac{1}{2} l\pi\right)}{(2n+1-l)!\left(4\pi f_\mathrm{c} T_\mathrm{p}\right)^l}, \\ v_{n,l} &= \frac{z_{n,l}}{(2n+2-l)} - \frac{(-1)^l}{(2n+2-l)!} \sum_{k=0}^{l} \frac{\cos\left(4\pi f_\mathrm{c} T_\mathrm{p} + \frac{1}{2} k\pi\right)}{(l-k)!\left(4\pi f_\mathrm{c} T_\mathrm{p}\right)^k}. \end{aligned}$$

Eq. (71) shows that Q_1^{O} is depending from the system parameters $E_\mathrm{p}^{\mathrm{O}}$, T_p, f_c, B as well as from the interference parameters P_J, B_J, f_J. In addition, concerning the special case $B_\mathrm{J} \to 0$, e.g., a cosine tone, r_ν has to be replaced with $r_\nu^m = \lim_{B_\mathrm{J}\to 0} r_\nu = \nu \Delta_{f_{\mathrm{c,J}}}^{\nu-1}$. Note that this result is consistent

to [9] if $P_N = 0$. In this case (71) simplifies to

$$\begin{aligned} Q_1^O = \frac{E_p^O P_J}{T_p \pi^2 \left(f_c^2 - f_J^2\right)^2} \Big[& f_c^2 + 3f_J^2 + \left(f_J^2 - f_c^2\right) \cos\left(4\pi f_c T_p\right) \\ & - 2f_J \left(f_J + f_c\right) \cos\left(2\pi \left(f_c - f_J\right) T_p\right) \\ & - 2f_J \left(f_J - f_c\right) \cos\left(2\pi \left(f_c + f_J\right) T_p\right) \Big]. \end{aligned} \tag{72}$$

The second order moment of the noise and interference-only part x_{jn}^O can be generally described as

$$Q_2^O = \int_{-t_1}^{T_p - t_1} \int_0^{T_p} \left[\left(P_N + P_J\right)^2 + 2\left(R_N(\tau) + R_J(\tau)\right)^2 \right] dt_1 d\tau. \tag{73}$$

Thereby, using the theorem of Price [44], (73) can be written in terms of the noise and interference related autocorrelation functions. With Parseval and the assumptions $2f_c \gg B$, $2f_J \gg B_J$ and $|f_c + f_J| \gg \left(B_J \text{ or } \left(B - B_J\right)\right)$ (73) results in

$$\begin{aligned} Q_2^O = 2T_p^2 \Bigg[& P_J^2 + P_J P_N + P_N^2 + \sum_{k=1}^{\infty} \frac{(-1)^k \left(2\pi T_p\right)^{2k} \left(P_J^2 B_J^{2k} + P_N^2 B_T^{2k}\right)}{(2k+1)!\,(2k+1)\,(k+1)} \\ & + \sum_{k=2}^{\infty} \frac{(-1)^k \left(2\pi T_p\right)^{2k-2} \left(P_J^2 B_J^{2k-2} + P_N^2 B_T^{2k-2}\right)}{(k)\,(2k)!} \Bigg] \\ & + \frac{2P_J P_N}{\pi B \left(f_p - f_m\right)} \sum_{k=0}^{\infty} \frac{(-1)^k (2\pi)^{2k+1} T_p^{2k+2}}{(2k+2)!} \cdot \left(\frac{f_1(k)}{2k+2} + \frac{f_2(k)}{2k+1} \right). \end{aligned} \tag{74}$$

Thereby, with $f_p = \frac{B}{2} + \frac{B_J}{2}$ and $f_m = \frac{B}{2} - \frac{B_J}{2}$, $f_1(k)$ and $f_2(k)$ are defined as:

$$\begin{aligned} f_1(k) = & \left(-f_m - \Delta_{f_{c,J}}\right)^{2k+2} - \left(-f_p - \Delta_{f_{c,J}}\right)^{2k+2} \\ & + \left(-f_m + \Delta_{f_{c,J}}\right)^{2k+2} - \left(-f_p + \Delta_{f_{c,J}}\right)^{2k+2} \end{aligned}$$

and

$$\begin{aligned} f_2(k) = & \left(f_p + \Delta_{f_{c,J}}\right) \left[\left(-f_m - \Delta_{f_{c,J}}\right)^{2k+1} - \left(-f_p - \Delta_{f_{c,J}}\right)^{2k+1} \right] \\ & + \left(f_p - \Delta_{f_{c,J}}\right) \left[\left(-f_m + \Delta_{f_{c,J}}\right)^{2k+1} - \left(-f_p + \Delta_{f_{c,J}}\right)^{2k+1} \right] \\ & + \left(f_p - f_m\right) \left[\left(f_m - \Delta_{f_{c,J}}\right)^{2k+1} - \left(-f_m - \Delta_{f_{c,J}}\right)^{2k+1} \right]. \end{aligned}$$

Q_2^O is influenced by the system parameters T_p, f_c, B as well as by the interference parameters P_J, B_J, f_J. However, in contrast to the second order moment Q_1^O it

cannot be reduced via $E_{\mathrm{p}}^{\mathrm{O}}$. Eq. (74) simplifies for $B_{\mathrm{J}} \to 0$ due to $P_{\mathrm{J}}^2 B_{\mathrm{J}}^{2k} = P_{\mathrm{J}}^2 B_{\mathrm{J}}^{2k-2} = 0$, $\frac{f_1(k)}{f_{\mathrm{p}}-f_{\mathrm{m}}} = (2k+2)\left[\left(-\frac{B}{2}-\Delta f_{\mathrm{c,J}}\right)^{2k+1} + \left(-\frac{B}{2}+\Delta f_{\mathrm{c,J}}\right)^{2k+1}\right]$ as well as $\frac{f_2(k)}{f_{\mathrm{p}}-f_{\mathrm{m}}} = (2k+1)\left(\frac{B}{2}+\Delta f_{\mathrm{c,J}}\right)\left(-\frac{B}{2}-\Delta f_{\mathrm{c,J}}\right)^{2k}$. Assuming $P_{\mathrm{N}} = 0$ (74) equals the result of [9]:

$$Q_2^{\mathrm{O}} = 2T_{\mathrm{p}}^2 P_{\mathrm{J}}^2 + \frac{P_{\mathrm{J}}^2}{8\pi^2 f_{\mathrm{J}}^2}\left[1 - \cos\left(4\pi f_{\mathrm{J}} T_{\mathrm{p}}\right)\right]. \tag{75}$$

BPPM: Considering BPPM the second order moment of the signal-noise and signal-interference part $x_{\mathrm{sjn}}^{\mathrm{P}}$ is: $Q_1^{\mathrm{P}} = \frac{1}{2}Q_1^{\mathrm{O}}$. Q_1^{P} differs from Q_1^{O} solely in a factor of two which can be ascribed to the reduced modulation specific pulse energy. In contrast to Q_1^{P} there is a significant difference concerning the second order moment of the noise and interference-only part $x_{\mathrm{jn}}^{\mathrm{P}}$. With the theorem of Price this can be generally described in terms of the noise and interference specific autocorrelation functions: ($\tau = t_1 - t_2$)

$$\begin{aligned} Q_2^{\mathrm{P}} = {} & 4\int_{-t_1}^{T_{\mathrm{p}}-t_1}\int_{0}^{T_{\mathrm{p}}}\left[R_{\mathrm{J}}^2(\tau) + R_{\mathrm{N}}^2(\tau) + R_{\mathrm{J}}(\tau)R_{\mathrm{N}}(\tau)\right]\mathrm{d}t_1\mathrm{d}\tau \\ & - 4\int_{-t_1}^{T_{\mathrm{p}}-t_1}\int_{\frac{T_{\mathrm{b}}}{2}}^{T_{\mathrm{p}}+\frac{T_{\mathrm{b}}}{2}}\left[R_{\mathrm{J}}^2(\tau) + R_{\mathrm{N}}^2(\tau) + R_{\mathrm{J}}(\tau)R_{\mathrm{N}}(\tau)\right]\mathrm{d}t_1\mathrm{d}\tau. \end{aligned} \tag{76}$$

Therefore, using the theorem of Parseval for $2f_{\mathrm{J}} \gg B_{\mathrm{J}}$, the closed-form result

$$\begin{aligned} Q_2^{\mathrm{P}} = {} & 2\sum_{k=1}^{\infty}\frac{(-1)^k(2\pi)^{2k}\left(P_{\mathrm{J}}^2 B_{\mathrm{J}}^{2k} + P_{\mathrm{N}}^2 B_{\mathrm{T}}^{2k}\right)g_{2k+2}}{(2k+1)!\,(2k+1)\,(k+1)} \\ & + \sum_{k=2}^{\infty}\frac{(-1)^k 2^{2k}(\pi)^{2k-2}\left(P_{\mathrm{J}}^2 B_{\mathrm{J}}^{2k-2} + P_{\mathrm{N}}^2 B_{\mathrm{T}}^{2k-2}\right)g_{2k}}{(2k)!\,(2k)} \\ & + \frac{2P_{\mathrm{J}}P_{\mathrm{N}}}{\pi B_{\mathrm{T}}\left(f_{\mathrm{p}}-f_{\mathrm{m}}\right)}\sum_{k=0}^{\infty}\frac{(-1)^k(2\pi)^{2k+1}g_{2k+2}}{(2k+2)!}\cdot\left(\frac{f_1(k)}{2k+2} + \frac{f_2(k)}{2k+1}\right) \end{aligned} \tag{77}$$

with

$$g_\nu = 2T_{\mathrm{p}}^\nu - \left(T_{\mathrm{p}} - \frac{T_{\mathrm{b}}}{2}\right)^\nu + 2\left(\frac{T_{\mathrm{b}}}{2}\right)^\nu - \left(T_{\mathrm{p}} + \frac{T_{\mathrm{b}}}{2}\right)^\nu$$

can be found. Q_2^{P} is influenced by the system parameters T_{p}, T_{b}, f_{c}, B as well as by the interference parameters P_{J}, B_{J}, f_{J}. Similar to Q_2^{O} it cannot be reduced via $E_{\mathrm{p}}^{\mathrm{P}}$. Eq. (77) reveals that for low data rates ($T_{\mathrm{b}} \to \infty$) $g_\nu \approx 2T_{\mathrm{p}}^\nu$ resulting in a negligible influence of Q_2^{P}. In contrast, the larger the data rate the higher its impact, e.g., for $T_{\mathrm{b}} = 2T_{\mathrm{p}}$ g_ν conducts to $g_\nu = 4T_{\mathrm{p}}^\nu - \left(2T_{\mathrm{p}}\right)^\nu$. In addition, for $B_{\mathrm{J}} \to 0$ and $P_{\mathrm{N}} = 0$, (77) allows the same simplifications as for

Q_2^{O}. In this case (77) conducts to

$$Q_2^{\mathrm{P}} = \frac{P_{\mathrm{J}}^2}{8\pi^2 f_{\mathrm{J}}^2}\left[2 - 2\cos\left(2\pi f_{\mathrm{J}} T_{\mathrm{b}}\right) + \cos\left(2\pi f_{\mathrm{J}}\left(T_{\mathrm{b}} - 2T_{\mathrm{p}}\right)\right)\right.$$
$$\left. - \; 2\cos\left(4\pi f_{\mathrm{J}} T_{\mathrm{p}}\right) + \cos\left(2\pi f_{\mathrm{J}}\left(T_{\mathrm{b}} + 2T_{\mathrm{p}}\right)\right)\right]. \tag{78}$$

4.1.3. Results

Based on the previous analysis the interference robustness of an OOK/BPPM based energy detection receiver can be identified. Thereby, assuming regulation of ECC [14] an MIR-UWB system with four subbands of equal bandwidth $B = 625\,\mathrm{MHz}$ is taken into account. Without loss of generality, the analysis focuses solely on the first subband located at $f_{\mathrm{c}} = 6.3125\,\mathrm{GHz}$. However, an extension to other subbands or other MIR-UWB system configurations, which are possibly based on other frequency masks is easily possible. Further common system parameters used in the following are the pulse duration $T_{\mathrm{p}} = 3.2\,\mathrm{ns}$, a mean transmit power normalized to one, the modulation specific pulse energy $E_{\mathrm{p}}^i, i \in \{\mathrm{O}, \mathrm{P}\}$ as well as a constant $\mathrm{SNR}_{\mathrm{E}} = 10\,\mathrm{dB}$ at the input of the energy detector. Fixed interference parameter is the interference specific bit duration $T_{\mathrm{b,J}} = 16T_{\mathrm{b}} = 102.4\,\mathrm{ns}$.

In Fig. 18 (a) the PG is plotted vs. the $\mathrm{SINR}_{\mathrm{E}}$ for the duty cycle $d_{\mathrm{s}} = \frac{1}{2}$. An interference with the two bandwidths $B_{\mathrm{J},1} = 20\,\mathrm{MHz}$ or $B_{\mathrm{J},2} = 400\,\mathrm{MHz}$ located at $f_{\mathrm{J}} = f_{\mathrm{c}} + 50\,\mathrm{MHz}$ is considered leading to the fixed duty cycles $d_{\mathrm{J},1} = \frac{1}{B_{\mathrm{J},1} T_{\mathrm{b,J}}} = 0.4883$ or $d_{\mathrm{J},2} = \frac{1}{B_{\mathrm{J},2} T_{\mathrm{b,J}}} = 0.0244$. For OOK/BPPM, the PG increases with higher $\mathrm{SINR}_{\mathrm{E}}$ up to the interference-free PG at $\mathrm{SNR}_{\mathrm{E}} = 10\,\mathrm{dB}$. Furthermore, it can be observed that the OOK/BPPM based PG varies with the interference bandwidth. For OOK, the PG increases with a larger interference bandwidth because of the minor impact of the mixed signal-interference as well as the interference-only component involved in the energy detection. A PG of energy detection can be achieved from an $\mathrm{SINR}_{\mathrm{E}} = -3.5\,\mathrm{dB}$ ($B_{\mathrm{J},1} = 20\,\mathrm{MHz}$) and from an $\mathrm{SINR}_{\mathrm{E}} = -5.5\,\mathrm{dB}$ ($B_{\mathrm{J},2} = 400\,\mathrm{MHz}$), respectively. For strong interference no PG results as the energy detector's decision variable is significantly corrupted. In contrast, for BPPM a PG can be achieved for small interference bandwidths, e.g., $B_{\mathrm{J},1} = 20\,\mathrm{MHz}$, over nearly the complete $\mathrm{SINR}_{\mathrm{E}}$ range. For $B_{\mathrm{J},2} = 400\,\mathrm{MHz}$ a PG occurs from $\mathrm{SINR}_{\mathrm{E}} = -2\,\mathrm{dB}$. The reason for this behaviour lies in a different amount of energy resulting from the mixed signal-interference and interference-only term within the two observation periods of duration T_{p}. Finally, the consideration of OOK/BPPM with respect to their relative PG shows that for strong NBI BPPM is more robust whereas OOK is more robust for mean and low interference.

The detector efficiency in terms of PG can be increased by increasing T_{b}, e.g., with multiples of T_{p}. This is illustrated in Fig. 18 (b) for $d_{\mathrm{s}} = \frac{1}{4}$. The enlargement of T_{b} via d_{s} results in an increase of E_{b} for fixed signal power. Thereby, the interference related second order moments Q_1^i and $Q_2^i, i \in \{\mathrm{O}, \mathrm{P}\}$ will be reduced as the interferer's energy is only collected during integration time T_{p} within T_{b}. Larger T_{b} can be implemented into an MIR-UWB transmitter with minor complexity. However, the trade-off to increase the detector's interference robustness is a reduction of data rate.

Fig. 19 (a) shows the PG of an OOK and BPPM specific energy detection vs. f_{J} for $d_{\mathrm{s}} = \frac{1}{2}$, which varies from $f_{\mathrm{c}} - \frac{B}{2}$ to $f_{\mathrm{c}} + \frac{B}{2}$ for fixed $\mathrm{SINR}_{\mathrm{E}} = 0\,\mathrm{dB}$, $\mathrm{SNR}_{\mathrm{E}} = 10\,\mathrm{dB}$, $T_{\mathrm{b,J}} = 102.4\,\mathrm{ns}$ as

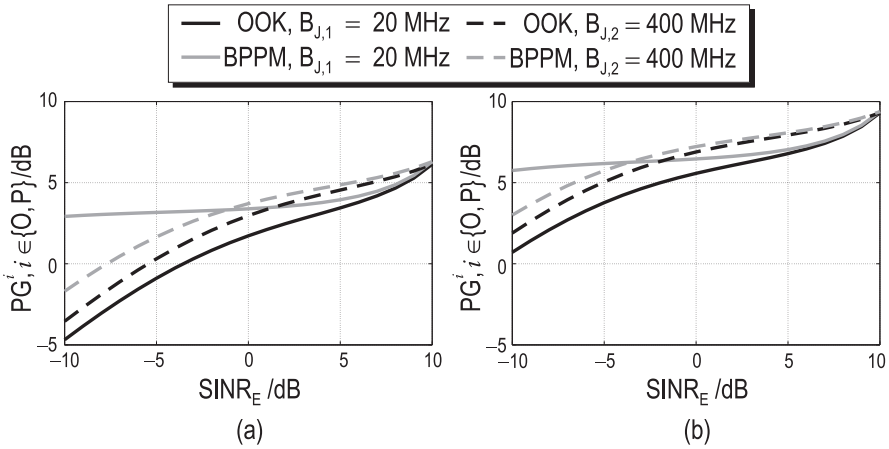

Figure 18. Processing gain of an OOK and BPPM specific energy detection vs. $\mathrm{SINR_E}$ with $B_{\mathrm{J},1} = 20\,\mathrm{MHz}$ and $B_{\mathrm{J},2} = 400\,\mathrm{MHz}$, $f_\mathrm{J} = f_\mathrm{c} + 50\,\mathrm{MHz}$, $\mathrm{SNR_E} = 10\,\mathrm{dB}$, $T_{\mathrm{b,J}} = 102.4\,\mathrm{ns}$, $d_\mathrm{J}\,(B_{\mathrm{J},1}) = 0.4883$ and $d_\mathrm{J}\,(B_{\mathrm{J},2}) = 0.0244$ for $T_\mathrm{b} = 2T_\mathrm{p}$ (a) and $T_\mathrm{b} = 4T_\mathrm{p}$ (b).

well as for $B_{\mathrm{J},1} = 20\,\mathrm{MHz}$ and $B_{\mathrm{J},2} = 400\,\mathrm{MHz}$. As long as the interference is completely inside the subband $T_{\mathrm{p,J}}$, d_J and hence P_J are fix. In particular, the modulation specific PG at $f_\mathrm{J} = f_\mathrm{c} + 50\,\mathrm{MHz}$ coincides with the one of Fig. 18. In addition, both modulation schemes show an increase of PG the more the interference is located at the subband's boundary ($f_\mathrm{J} = f_\mathrm{c} \pm \frac{1}{T_\mathrm{p}}$). This can be on one hand ascribed to the subband pulse's sinc spectrum which is zero at the subband's boundary. On the other hand, the more f_J is located at the subband's boundary the minor the interference bandwidth falling into the subband. In case interference overlaps with the subband's boundary, the effective interference parameters B_J, f_J and d_J changes resulting in a reduction of the actual interference power P_J. Fig. 19 (b) shows again that a significant increase of the modulation specific PG can be achieved for $d_\mathrm{s} = \frac{1}{4}$. However, without proper pulse shaping the increase depends strongly on the interferer's position inside the subband.

4.2. Coexistence-based approaches

The MIR-UWB system has no exclusive frequency range within the available transmission bandwidth. For this reason there is an increased interference potential from a possible large number of radio systems operating in the same frequency domain. As shown in [12] the impact of interference can result in a significant decrease of the bit error rate (BER) performance of the MIR-UWB system. To maintain system performance, the following section gives a short overview of various coexistence-based approaches with respect to an efficient and easy-to-realise interference mitigation.

Coexistence-based approaches aim at the reliable on-line mitigation of interferences which occur in the environment of the MIR-UWB system. Thus, a best possible trade-off between a maximum data rate and a minimum BER can be obtained for arbitrary interference situations. In this context, an essential requirement is the integration of coexistence-based approaches into the existing MIR-UWB system with only minor complexity increase. Thus, the MIR-UWB system configuration should not be changed in presence of interference on one hand; on

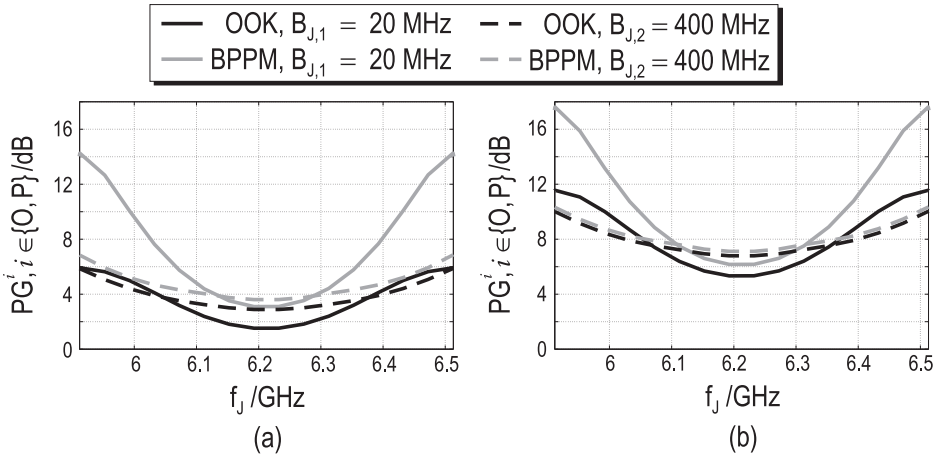

Figure 19. Processing gain of an OOK and BPPM specific energy detection vs. f_J for $\mathrm{SINR_E} = 0\,\mathrm{dB}$, $\mathrm{SNR} = 10\,\mathrm{dB}$, $B_{\mathrm{J},1} = 20\,\mathrm{MHz}$, $B_{\mathrm{J},2} = 400\,\mathrm{MHz}$ and $T_{\mathrm{b,J}} = 102.4\,\mathrm{ns}$ for $T_\mathrm{b} = 2T_\mathrm{p}$ (a) as well as $T_\mathrm{b} = 4T_\mathrm{p}$ (b).

the other hand it should be possible to realise coexistence without complex estimations of interference specific parameters such as the interference power, the interference bandwidth, the interference carrier frequency or the number of instantaneous available interferences.

4.2.1. Static coexistence approach

From a complexity point of view a static coexistence approach should be used. Thereby interfered subbands are deactivated by means of the system specific band plan before any data transmission occurs. Best trade-off between system performance and effort for interference handling will be achieved. However, this approach does not consider dynamic interference situations and hence does not contribute to efficient spectrum usage. Therefrom, the necessity for further efficient and low complex, but more flexible alternatives arises.

4.2.2. Detect and Avoid (DAA)

In [6, 34] an easy-to-realise DAA approach is presented allowing a reliable detection of temporary NBI after system initialisation or within data transmission.

For this purpose, the regularly transmitted preamble is adjusted to simultaneous subband specific signal and noise energy estimation used by the DAA approach. Thereby, a static interference-free working point (WP) is defined, ensuring a determinated BER in each subband. After initialisation, the estimated SNRs are compared with the WP, leading to subband deactivation, if the SNR is lower than the WP. Otherwise, the subband is (re)enabled for data transmission.

During data transmission, the initially estimated signal and noise energy values of enabled subbands are recursively updated in dependence of the actual subband specific bit decision to adapt the initial decision threshold. In addition, this process allows the possibility of fast and reliable detection of suddenly weak or strong interfered subbands. For this reason,

a characteristic weighting factor k is used to manipulate the instantaneous energy value's influence on the recursive estimation. Simulation results [6] show a robust interference detection with only a marginal BER performance loss for $k = 10$.

4.2.3. Image-based thresholding

In [10], a simple cluster-based coexistence approach (coexistence approach 1) is analysed resulting in a decision threshold ϵ_{th} with respect to interfered or not interfered noise energy values. Based on the image-based thresholding method of [41] occupied time-frequency slots can be automatically detected and recorded within an extended time-frequency band plan used for initialisation or data transmission.

Assuming knowledge of the interferers' periodicity and perfect synchronisation, m_0 binary zeros are sent over each subband $i \in \{1, \ldots, N_{\text{sub}}\}$. The measured energy values are written as an energy matrix $\underline{X} = \left[x_{j,i}\right], j = 1, \ldots, m_0, i = 1, \ldots, N_{\text{sub}}$ and assigned to their nearest quantized energy levels $E_{\min} = \epsilon_1 < \epsilon_2 < \ldots < \epsilon_U = E_{\max}$. Thereby, $E_{\min}$ and $E_{\max}$ stands for the minimum and the maximum occurring energy value in $\underline{X}$. The allocation leads to an energy distribution, which is described as

$$p_i = \frac{n_i}{m_0 N_{\text{sub}}}, i \in 1, \ldots, U. \tag{79}$$

To obtain a separation between interfered and not interfered energy values, two energy classes $C_0 = \{\epsilon_1, \ldots, \epsilon_u\}$ and $C_1 = \{\epsilon_{u+1}, \ldots, \epsilon_U\}$ can be defined, which include interfered and not interfered energy values (Fig. 20 (a))

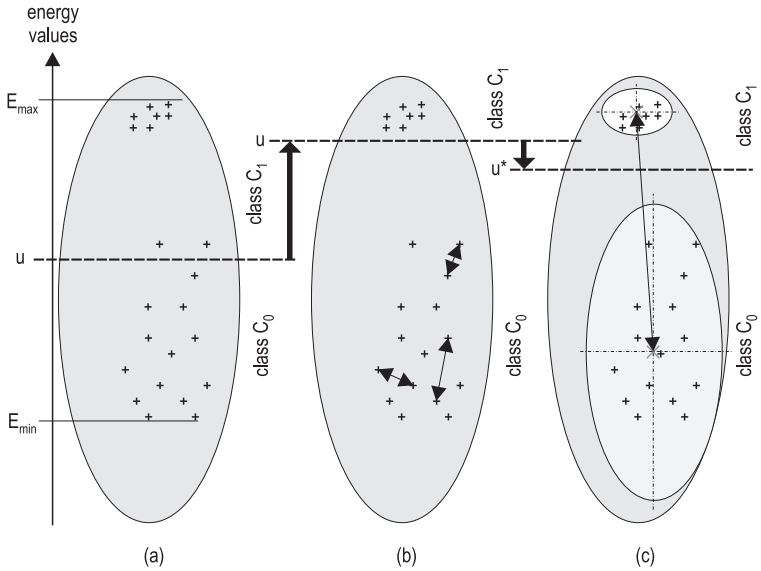

Figure 20. Energy classes, threshold determination. Sub-figure (a) shows the average of all values, sub-figure (b) optimizes according to eq. (81) and sub-figure (c) according to eq. (84).

In order to classify energy values, index u has to be determined using two optimisation criteria.

The first optimisation criterion consists of the minimisation of the combined empirical energy class variance

$$s_{\mathrm{w}}^2(u) = s_{\mathrm{C}_0}^2(u)\, P_{\mathrm{C}_0}(u) + s_{\mathrm{C}_1}^2(u)\, P_{\mathrm{C}_1}(u). \tag{80}$$

This step aims at an adjustment of the initially set index u, whereas a correct allocation of energy outliers to the corresponding other class is achieved (Fig. 20 (b)). It is based on a weighted sum of the classes' occurrence probabilities

$$P_{\mathrm{C}_0}(u) = \sum_{i=1}^{u} p_i, \qquad P_{\mathrm{C}_1}(u) = 1 - P_{\mathrm{C}_0}(u), \tag{81}$$

as well as on the empirical energy classes' variances

$$s_{\mathrm{C}_l}^2(u) = \begin{cases} \sum\limits_{i=1}^{u} \left(\epsilon_i - \bar{x}_{\mathrm{C}_l}(u)\right)^2 \frac{p_i}{P_{\mathrm{C}_l}(u)}, & l = 0 \\ \sum\limits_{i=u+1}^{U} \left(\epsilon_i - \bar{x}_{\mathrm{C}_l}(u)\right)^2 \frac{p_i}{P_{\mathrm{C}_l}(u)}, & l = 1 \end{cases} \tag{82}$$

with

$$\bar{x}_{\mathrm{C}_l}(u) = \begin{cases} \sum\limits_{i=1}^{u} \frac{\epsilon_i p_i}{P_{\mathrm{C}_l}(u)}, & l = 0 \\ \sum\limits_{i=u+1}^{U} \frac{\epsilon_i p_i}{P_{\mathrm{C}_l}(u)}, & l = 1 \end{cases} \tag{83}$$

describing the empirical energy class mean levels.

The second optimisation criterion considers the maximisation of the empirical variance between both energy classes

$$s_{\mathrm{b}}^2(u) = \left(\bar{x}_{\mathrm{C}_0}(u) - \bar{x}_{tot}\right)^2 P_{\mathrm{C}_0}(u) + \left(\bar{x}_{\mathrm{C}_1}(u) - \bar{x}_{tot}\right)^2 P_{\mathrm{C}_1}(u) \tag{84}$$

standing for the weighted variance of the energy class means $\bar{x}_{\mathrm{C}_i}, i = 0, 1$ themselves around the total mean $\bar{x}_{\mathrm{tot}} = \bar{x}_{\mathrm{C}_0} + \bar{x}_{\mathrm{C}_1}$ of the time-frequency pattern (Fig. 20 (c)). Hence, a separation of both classes with respect to the mean value of the total time-frequency pattern is obtained, leading to a more accurate adaptation of index u.

As both optimisation criteria have opposing effects with respect to the best index $u^\star$, they are combined into one characteristic optimisation criterion which is defined as [41]:

$$u^\star = \arg \max_{u=1,\ldots,U} \frac{s_{\mathrm{b}}^2(u)}{s_{\mathrm{w}}^2(u)}. \tag{85}$$

This leads to an adjustment of the initially arbitrary index u. Thereby, a correct allocation of energy outliers to the corresponding energy classes is achieved. Evaluated index $u^\star$ leads to interference detection threshold $\epsilon_{\mathrm{th}} = \epsilon_{u^\star}$. Afterwards a binary decision has to be done for all

received energy values $x_{j,i}, j = 1, \ldots, m_0, i = 1, \ldots, N_{\text{sub}}$, which are logged in band plan $\underline{L}$. In this context, we define an energy cell as interfered if $x_{j,i} \geq \epsilon_{\text{th}}$.

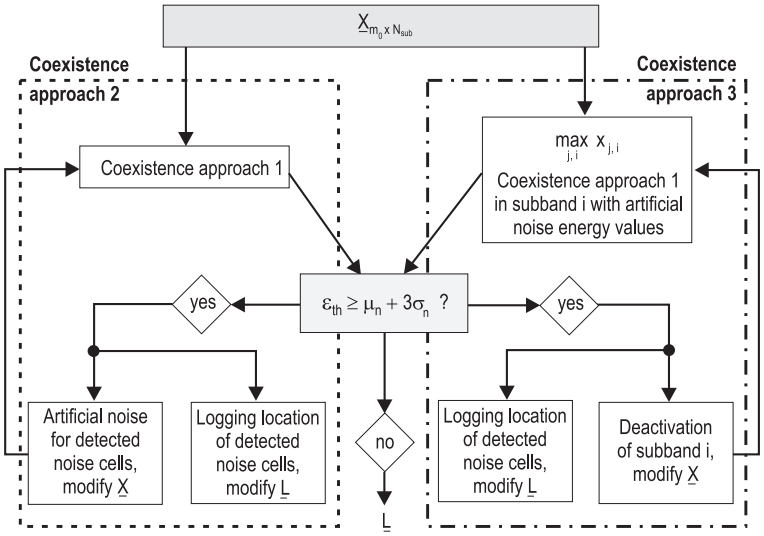

Figure 21. Schematic procedure of global iterative method (coexistence approach 2) and local hierarchical method (coexistence approach 3).

Since the main drawback of the global coexistence approach is its reduced efficiency in case of simultaneously operating broad- or narrowband interference, it should be improved by using iterative coexistence methods [12]. In a global iterative method (coexistence approach 2, left side of Fig. 21) the plausibility of the resulting interference detection threshold is verified via the $3\sigma_{\text{n}}$ standard deviation termination criterion

$$\epsilon_{\text{th}} \overset{?}{\geq} \mu_{\text{n}} + 3\sigma_{\text{n}} \tag{86}$$

for which Gaussian distribution as well as an interference-free noise source $n(t)$ with mean μ_{n} and standard deviation σ_{n} is assumed at the receiver side. If ϵ_{th} exceeds the confidence interval, deactivation flags are logged within the band plan.

Simultaneously, all labelled possibly corrupted noise energy values are replaced with artificially generated noise energy values resulting from the noise source mentioned above. This procedure is iteratively repeated until the termination criterion is achieved. In this case, the final iterative band plan is delivered and used for initialisation and data transmission.

In contrast, a local hierarchical iterative method (coexistence approach 3, right side of Fig. 21) handles every subband individually to achieve a local based interference detection threshold. The subband with maximum occurring energy value is identified and delivered to receiver side interference detection in conjunction with a sufficient number of additional artificial noise energy values of the above mentioned noise source. For the detection of the coexistence approach's termination, the $3\sigma_n$ standard deviation is used again. If the interference threshold lies above the confidence interval, detected noise cells of the considered subband are labelled

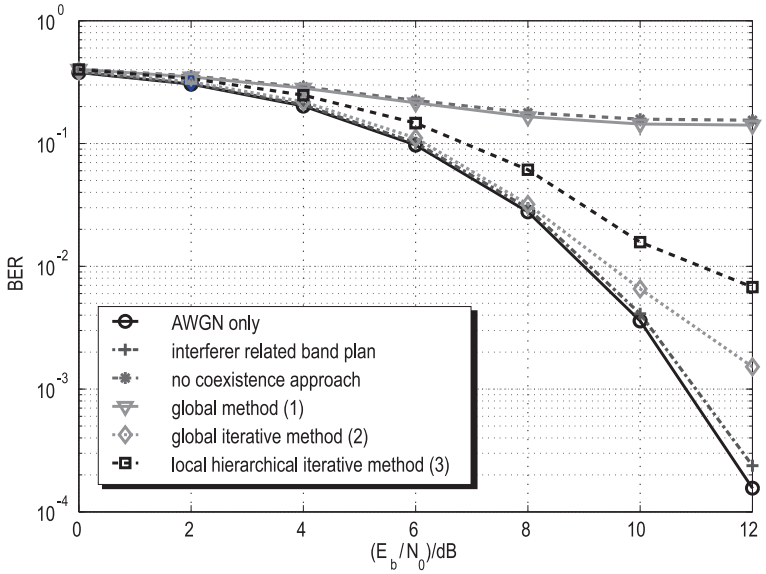

Figure 22. BER vs. E_b/N_0 for AWGN and fixed SIRs of -10 dB (IEEE 802.11a WLAN [47]), 0 dB and 5 dB (IEEE 802.15.3a MB OFDM UWB 1 and 2 [2]) regarding an interferer related band plan, no coexistence approach and the coexistence approaches 1 to 3 [12].

within the band plan. In parallel, the corresponding subband is deactivated and the procedure is iteratively repeated. If the coexistence approach terminates, the binary band plan is allocated to the transmitter for initialisation and data transmission.

Performance analysis [12] demonstrates the high capability of both iterative coexistence methods in presence of multiple interferers having the same or different interference powers (Fig. 22).

4.3. Narrowband interference mitigation

The MIR-UWB system is characterised by a particular high vulnerability to NBI as all interferences inside the passband of the analogue front-end are considered by the energy detection receiver. Its performance can decrease significantly resulting in an increase of the error probability. Hence, a crucial issue concerns the efficient mitigation of NBI [58].

This section analyses the potential of the non-linear Teager-Kaiser (TK) operation [22] to mitigate NBI without the knowledge of the interference related carrier frequency. Based on the definition of the TK operation and some of its most important properties the mitigation potential of a TK based energy detector is analysed. In this context a modified TK operation is introduced and compared with the traditional TK operation [8]. The analysis of the traditional and the modified TK operation considers first one narrowband signal in the baseband. Finally, the analysis is extended to the bandpass domain for one and multiple NBI [5]. Thereby, the potential to integrate the TK operation into the existing MIR-UWB system is discussed for one NBI. Based on the proposal of [42] it is shown that the integration can be realised with only minor complexity increase.

4.3.1. Teager-Kaiser operation

The continuous TK operation is a non-linear differential operator of order two defined as

$$\Psi\left(x\left(t\right)\right) = \dot{x}^2\left(t\right) - x\left(t\right)\ddot{x}\left(t\right). \tag{87}$$

To illustrate the effectiveness of the TK operation the harmonic oscillation $x\left(t\right) = A\cos\left(\omega_0 t + \phi_0\right)$ is considered. Using (87) the signal at the output of the TK operation can be described as

$$\Psi\left(x\left(t\right)\right) = A^2\omega_0^2\left(\sin^2\left(\omega_0 t + \phi_0\right) + \cos^2\left(\omega_0 t + \phi_0\right)\right) = A^2\omega_0^2.$$

Hence, for the special case of a simple harmonic oscillation the TK operation leads to a frequency shift to DC. Fig. 23 highlights the spectrum of a harmonic oscillation (a) as well as the resulting spectrum at the output of TK operation (b).

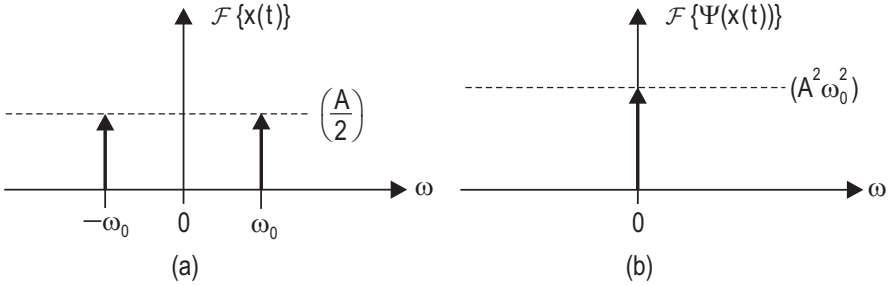

Figure 23. Effectiveness of TK operation for the harmonic oscillation $x\left(t\right) = A\cos\left(\omega_0 t + \phi_0\right)$.

An interpretation of this behaviour is given in [22]. In case of a harmonic oscillation the output of the TK operation describes the required energy to generate the oscillation. Considering (88) the energy depends not only by the amplitude A but also by the oscillation frequency ω_0. Thus, for a constant A the required energy to generate an exemplary 10 Hz signal is lower than the one of an 1000 Hz signal.

When using the continuous TK operation of (87) basic operator specific rules have to be generally considered. A detailed description can be found in [23]. In context with interference mitigation the most important property can be the behaviour of the TK operation in presence of several overlapping signals. In case of K_S overlapping signals $x_1\left(t\right)$, $x_2\left(t\right)$, ..., $x_{K_S}\left(t\right)$ the resulting signal at the output of TK operation conducts to

$$\Psi\left(\sum_{i=1}^{K_S} x_i\left(t\right)\right) = \sum_{i=1}^{K_S}\Psi\left(x_i\left(t\right)\right) + \sum_{j=1}^{K_S-1}\sum_{i=j+1}^{K_S}\Psi_c\left(x_j\left(t\right), x_i\left(t\right)\right). \tag{88}$$

It consists on one hand of K_S summands describing the TK operation of the signals $x_1\left(t\right)$, $x_2\left(t\right)$, ..., $x_{K_S}\left(t\right)$. Furthermore, due to the non-linearity of the TK operation the additional cross component

$$\begin{aligned}\Psi_c\left(x_j\left(t\right), x_i\left(t\right)\right) &= \Psi_{c_j}\left(x_j\left(t\right), x_i\left(t\right)\right) + \Psi_{c_i}\left(x_i\left(t\right), x_j\left(t\right)\right)\\ &= 2\dot{x}_j\left(t\right)\dot{x}_i\left(t\right) - x_j\left(t\right)\ddot{x}_i\left(t\right) - x_i\left(t\right)\ddot{x}_j\left(t\right)\end{aligned} \tag{89}$$

occurs. This component considers the mutual influence of the two signals $x_j(t)$ and $x_i(t)$. It is composed of the generally non-symmetric signal parts $\Psi_{c_1}(x_1(t), x_2(t)) = \dot{x}_1(t)\dot{x}_2(t) - x_1(t)\ddot{x}_2(t)$ and $\Psi_{c_2}(x_2(t), x_1(t)) = \dot{x}_2(t)\dot{x}_1(t) - x_2(t)\ddot{x}_1(t)$. From (89) two special cases can be immediately concluded. Firstly, the cross component $\Psi_c(x(t), x(t)) = 2\Psi(x(t))$ if $x(t)$ is overlapped with itself. Secondly, $\Psi_c(a, x(t)) = -a\ddot{x}(t)$. The cross component of a constant a and a signal $x(t)$ can be expressed as the product of a with the second derivative of $x(t)$. In particular, the cross component disappears completely, if $a = 0$.

The TK operation of (87) can be modified with the weighting factor $k \neq 0$ as follows [8]:

$$\Psi_k(x(t)) = k\dot{x}(t)^2 - x(t)\ddot{x}(t). \tag{90}$$

This definition contains the traditional TK operation if $k = 1$. Thereby, the Fourier transform of $\Psi_k(x(t))$ of a signal $x(t)$ is generally given as

$$\mathcal{F}\{\Psi_k(x(t))\} = 4\pi^2\left(X(f) * f^2X(f) - kfX(f) * fX(f)\right). \tag{91}$$

Considering again the special case of a harmonic oscillation $x(t) = A\cos(\omega_0 t)$ the Fourier transform conducts to

$$\mathcal{F}\{\Psi_k(x(t))\} = \frac{1}{2}A^2(2\pi f_0)^2\left((k+1)\delta(f) + \frac{1}{2}(1-k)(\delta(f+2f_0) + \delta(f-2f_0))\right). \tag{92}$$

The effectiveness of the modified TK operation is highlighted in Fig. 24.

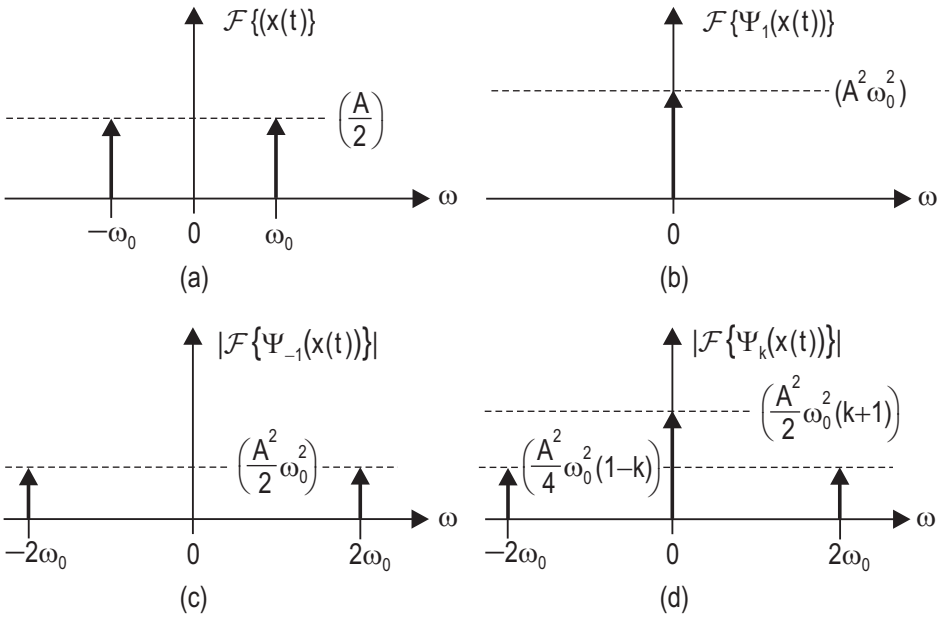

Figure 24. Effectiveness of the traditional and the modified TK operation for $x(t) = A\cos(\omega_0 t)$.

In contrast to the traditional TK operation (Fig. 24 (b)) additional spectral parts at $2\omega_0$ can be observed for $k \neq 1$ (Fig. 24 (d)). For the special case $k = -1$ the complete energy is even shifted to this frequency (Fig. 24 (c)). Hence, it can be concluded that a modified TK operation operates not only as DC frequency shifter.

Due to the modification of the TK operation the property of overlapping signals changes. If two signals $x_1(t)$ and $x_2(t)$ occur at the input of the TK operation its output conducts to [8]:

$$\Psi_k(x_1(t) + x_2(t)) = \Psi_k(x_1(t)) + \Psi_k(x_2(t)) + \Psi_k^{\mathrm{c}}(x_1(t), x_2(t)), \tag{93}$$

where

$$\Psi_k^{\mathrm{c}}(x_1(t), x_2(t)) = 2k\dot{x}_1(t)\dot{x}_2(t) - x_1(t)\ddot{x}_2(t) - x_2(t)\ddot{x}_1(t) \tag{94}$$

stands for the modified cross component of $x_1(t)$ and $x_2(t)$.

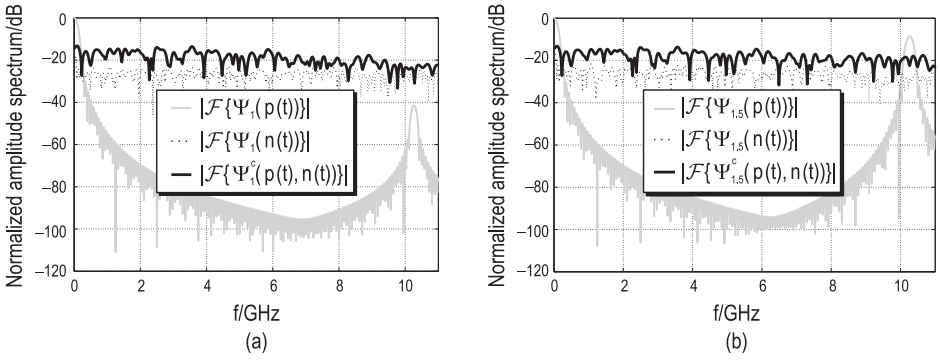

Figure 25. Normalized amplitude spectrum at the output of the traditional TK operation for $k = 1$ (a) and $k = 1.5$ (b), $E_{\mathrm{b}}/N_0 = 12\,\mathrm{dB}$.

Fig. 25 shows the difference of the traditional (a) and the modified TK operation (b) for OOK in case of a binary one. Thereby, Fig. 25 (a) highlights the normalized amplitude spectrum of the occurring components for the interference-free AWGN case for $k = 1$ and $E_{\mathrm{b}}/N_0 = 12\,\mathrm{dB}$. The considered pulse is a cosine-shaped pulse with pulse duration $T = 12.8\,\mathrm{ns}$ and carrier frequency $f_{\mathrm{c}} = 5.13\,\mathrm{GHz}$ [8]. Obviously, the TK operation mixes a large signal part of the pulse to around DC. However, a minor contribution around $2f_{\mathrm{c}}$ can also be observed. As this contribution is much lower than the spectral contributions of $\Psi_1(n(t))$ and $\Psi_1^{\mathrm{c}}(p(t), n(t))$ a possible detection may be limited to the frequency range around DC.

In contrast, Fig. 25 (b) illustrates that the modification of the TK operation with, e.g. $k = 1.5$, has the potential to improve the detection for AWGN. Also in this case large pulse related spectral contributions around DC occur. Furthermore, a significant increase of $\approx 30\,\mathrm{dB}$ of the pulse's amplitude spectrum $\mathcal{F}\{\Psi_{1,5}(p(t))\}$ occurs around $2f_{\mathrm{c}}$. The resulting amplitude spectrum of the pulse is both around DC and around $2f_{\mathrm{c}}$ larger than the contributions of $\Psi_{1.5}(n(t))$ and $\Psi_{1.5}^{\mathrm{c}}(p(t), n(t))$. Hence, an improved detection performance can be expected for AWGN if frequencies around DC as well as around $2f_{\mathrm{c}}$ are considered.

The reason for this behaviour can be ascribed to the modified TK operation of the pulse. Assuming negligible influences of the first and the second derivative of $p(t)$ at $|t| = \frac{T}{2}$ the output of the TK operation on $p(t)$ can be described as [8]:

$$\begin{aligned}\Psi_k\left(p\left(t\right)\right) = \frac{2}{3T}\Big[&0.5\left(k+1\right)\left(\omega_{\mathrm{T}}^2+3\omega_{\mathrm{c}}^2\right)\\ &-0.25\left(k-1\right)\left(\omega_{\mathrm{T}}-\omega_{\mathrm{c}}\right)^2\cos\left(2\left(\omega_{\mathrm{c}}-\omega_{\mathrm{T}}\right)t\right)\\ &+0.5\left(\left(k+1\right)\omega_{\mathrm{T}}^2-3\left(k-1\right)\omega_{\mathrm{c}}^2\right)\cos\left(2\omega_{\mathrm{c}}t\right)\\ &+\left(0.5\omega_{\mathrm{T}}^2+\left(k-1\right)\left(\omega_{\mathrm{c}}\omega_{\mathrm{T}}-\omega_{\mathrm{c}}^2\right)\right)\cos\left(\left(2\omega_{\mathrm{c}}-\omega_{\mathrm{T}}\right)t\right)\\ &+\left(0.5\omega_{\mathrm{T}}^2-\left(k-1\right)\left(\omega_{\mathrm{c}}\omega_{\mathrm{T}}+\omega_{\mathrm{c}}^2\right)\right)\cos\left(\left(2\omega_{\mathrm{c}}+\omega_{\mathrm{T}}\right)t\right)\\ &-0.25\left(k-1\right)\left(\omega_{\mathrm{T}}+\omega_{\mathrm{c}}\right)^2\cos\left(2\left(\omega_{\mathrm{c}}+\omega_{\mathrm{T}}\right)t\right)\\ &+0.5\left(\omega_{\mathrm{c}}^2\left(k+1\right)-\omega_{\mathrm{T}}^2\left(k-1\right)\right)\cos\left(2\omega_{\mathrm{T}}t\right)\\ &+\left(2\omega_{\mathrm{c}}^2\left(k+1\right)+\omega_{\mathrm{T}}^2\right)\cos\left(\omega_{\mathrm{T}}t\right)\Big]\end{aligned} \tag{95}$$

with $\omega_{\mathrm{T}} = \frac{2\pi}{\mathrm{T}}$ and $\omega_{\mathrm{c}} = 2\pi f_{\mathrm{c}}$. Obviously, a modification of the TK operation leads to additional spectral parts at its output. Hence, it is possible to influence the distribution of pulse energy via a simple weighting of the TK operation. It should be noted that the traditional as well as the modified TK operation acts not only as a frequency-to-DC shifter due to additional spectral parts around $2f_{\mathrm{c}}$. For the traditional TK operation ($k = 1$) the two spectral components at $2\left(\omega_{\mathrm{c}}-\omega_{\mathrm{T}}\right)$ and $2\left(\omega_{\mathrm{c}}+\omega_{\mathrm{T}}\right)$ disappear completely resulting in a lower energy concentration around $2f_{\mathrm{c}}$.

4.3.2. Mitigation potential of Teager-Kaiser operation

Assuming negligible noise this section analyses the potential of the traditional and the modified TK operation to mitigate NBI. For this the TK operation's effectiveness is first described in the baseband. Afterwards it is extended to the bandpass domain.

Baseband Domain

To make statements on the effectiveness of the TK operation for a narrowband signal we first consider a narrowband baseband signal of bandwidth $2\omega_N$ which can be modelled as

$$j\left(t\right) = \sum_{i=1}^{N} A_i \sin\left(\omega_i t + \phi_i\right). \tag{96}$$

It consists of N overlapping sinusoids of amplitudes $A_i, i = 1,\ldots,N$, of phases $\phi_i, i = 1,\ldots,N$ as well as of frequencies $\omega_i = 2\pi f_i, i = 1,\ldots,N$. Given to the modified TK operation its output can be described for $\phi_i = 0, i = 1,\ldots,N$ as[3]

$$\Psi_k\left(j\left(t\right)\right) = C_k\left(t\right) + \sum_{i=1}^{N}\sum_{j>i}^{N} z_i^j \cos\left(\left(\omega_i-\omega_j\right)t\right) + z_j^i \cos\left(\left(\omega_i+\omega_j\right)t\right), \tag{97}$$

[3] The TK operation is generally characterised by a strong phase dependency. To simplify the descriptions we only consider the special case $\phi_i = 0, i = 1,\ldots,N$ in the following.

with

$$C_k(t) = \frac{1}{2}\sum_{i=1}^{N} A_i^2\omega_i^2\left[(k+1)+(k-1)\cos(2\omega_i t)\right],$$
$$z_i^j = kA_iA_j\omega_i\omega_j + \frac{1}{2}A_iA_j\omega_i^2 + \frac{1}{2}A_iA_j\omega_j^2$$

and

$$z_j^i = kA_iA_j\omega_i\omega_j - \frac{1}{2}A_iA_j\omega_i^2 - \frac{1}{2}A_iA_j\omega_j^2.$$

For the traditional TK operation ($k = 1$) the resulting signal is composed of the DC component $C_1 = \sum_{i=1}^{N} A_i^2\omega_i^2$. In addition, further components around $\omega_i - \omega_j$ and $\omega_i + \omega_j$ occur. Its quantity depends on the two factors $z_i^j = 0,5A_iA_j\left(\omega_i+\omega_j\right)^2$ and $z_j^i = -0,5A_iA_j\left(\omega_i-\omega_j\right)^2$. Thereby, a higher energy concentration can be observed for lower frequencies. In contrast, the modified TK operation ($k \neq 1$) shows spectral contributions around DC, around $\omega_i + \omega_j$ and $\omega_i - \omega_j$ as well as around $2\omega_i, i = 1,\ldots,N$. In particular, the contributions at $\omega_i + \omega_j$ and $\omega_i - \omega_j$ are influenced with larger weighting factors z_i^j and z_j^i. Hence, using the modified TK operation a high energy concentration still occurs for low frequencies. However, due to the additional spectral components at $2\omega_i, i = 1,\ldots,N$ the relative difference of energy concentration reduces.

Bandpass Domain

NBI influencing the MIR-UWB system operates in the bandpass domain. Based on the insight for a baseband signal an analytical description of the effectiveness of the traditional and the modified TK operation is done for one or more narrowband bandpass signals. Due to analytical tractability it is assumed that the lth bandpass signal can be described as

$$\begin{aligned} j_l(t) &= 2A_l\sum_{i=1}^{N_l}\sin\left(\omega_{l,i}t\right)\cos\left(\omega_{c_l}t\right) \\ &= \underbrace{A_l\sum_{i=1}^{N_l}\sin\left(\left(\omega_{c_l}+\omega_{l,i}\right)t\right)}_{\alpha_l(t)} - \underbrace{A_l\sum_{i=1}^{N_l}\sin\left(\left(\omega_{c_l}-\omega_{l,i}\right)t\right)}_{\beta_l(t)}. \end{aligned} \tag{98}$$

The bandpass signal $j_l(t)$ of amplitude $2A_l$ consists of N_l sinusoids of frequencies $\omega_{l,1} < \omega_{l,2} < \ldots < \omega_{l,N_l}, \omega_{l,i} = 2\pi f_{l,i}, i = 1,\ldots,N_l$ located around the carrier frequency $\omega_{c_l} = 2\pi f_{c_l}$ with the bandwidth $B_l = 2\omega_{N_l}$.

If K_S bandpass signals $j_l(t), l = 1,\ldots,K_S$ are present at the input of TK operation its output can be described as

$$\Psi_k\left(\sum_{l=1}^{K_S} j_l(t)\right) = \sum_{l=1}^{K_S}\Psi_k\left(j_l(t)\right) + \Psi_{k,m}^{c}(t). \tag{99}$$

It consists of the components $\Psi_k\left(j_l(t)\right) = \Psi_k\left(\alpha_l(t)\right) + \Psi_k\left(\beta_l(t)\right) + \Psi_k^c\left(\alpha_l(t),\beta_l(t)\right), l = 1,\ldots,K_S$ which always occur in presence of one bandpass signal. Assuming $\omega_{c_l} \gg B_l$ the lth

bandpass signal $j_l(t), l = 1, \ldots, K_S$ results in [8]

$$\begin{aligned}
&\Psi_k(j_l(t)) \approx \\
&\quad A_l^2 \omega_{c_l}^2 \sum_{u=1}^{N_l} \left[(k+1) + 0.5(k-1) \cdot \left[\cos\left(2\left(\omega_{c_l} - \omega_{l,u}\right)t\right) + \cos\left(2\left(\omega_{c_l} + \omega_{l,u}\right)t\right)\right]\right] \\
&+ A_l^2 \omega_{c_l}^2 \sum_{u=1}^{N_l} \sum_{v>u}^{N_l} \left[2(k+1)\cos\left(\left(\omega_{l,u} - \omega_{l,v}\right)t\right) + (k-1)\cos\left(\left(2\omega_{c_l} + \omega_{l,u} + \omega_{l,v}\right)t\right)\right. \\
&\qquad\qquad \left. + (k-1)\cos\left(\left(2\omega_{c_l} - \omega_{l,u} - \omega_{l,v}\right)t\right)\right] \\
&- A_l^2 \omega_{c_1}^2 \sum_{u=1}^{N_l} \sum_{v=1}^{N_l} \left[(k+1)\cos\left(\left(\omega_{l,u} + \omega_{l,v}\right)t\right) - (k-1)\cos\left(\left(2\omega_{c_l} + \omega_{l,u} - \omega_{l,v}\right)t\right)\right]. \quad (100)
\end{aligned}$$

This result reveals that the traditional TK operation ($k = 1$) acts as a frequency-to-DC shifter for each bandpass signal $j_l(t), l = 1, \ldots, K_S$. In this case the corresponding spectral range goes from DC to the largest occurring bandwidth $B_l, l = 1, \ldots, K_S$ of the K_S bandpass signals. For the modified TK operation additional spectral components around $2\omega_{c,l}, l = 1, \ldots, K_S$ occur. For this reason a mitigation of NBI by the modified TK operation is critical. Finally, for the special case $k = -1$ the complete energy is shifted to $2\omega_{c,l}, l = 1, \ldots, K_S$. This confirms the statement that energy parts can be shifted between frequency ranges with a modified TK operation.

If the output of the traditional or the modified TK operation would only consist of components from $\Psi_k(j_l(t)), l = 1, \ldots, K_S$ a mitigation of the K_S bandpass signal could be possible as $B_T \gg B_l, l = 1, \ldots, K_S$. However, as can be seen in (99), the additional signal component

$$\Psi_{k,m}^c(t) = \sum_{r=1}^{K_S-1} \sum_{l=r+1}^{K_S} \left[\Psi_k^c(\alpha_r(t), \alpha_l(t)) + \Psi_k^c(\beta_r(t), \beta_l(t))\right] + \sum_{r=1}^{K_S} \sum_{l \neq r} \Psi_k^c(\alpha_r(t), \beta_l(t)) \quad (101)$$

occurs in case of at least two bandpass signals. The component $\Psi_{k,m}^c(t)$ describes the cross components between different bandpass signals $j_l(t)$ and $j_r(t), l \neq r$. Thereby, assuming $\omega_{c_l} \gg B_l$ and $\omega_{c_r} \gg B_r$ the two cross components can be described as

$$\begin{aligned}
&\Psi_k^c(\alpha_r(t), \alpha_l(t)) + \Psi_k^c(\beta_r(t), \beta_l(t)) \approx \\
&\sum_{u=1}^{N_r} \sum_{v=1}^{N_l} Z_{1,k} \left[\cos\left(\left(\omega_{c_r} - \omega_{c_l} + \omega_{r,u} - \omega_{l,v}\right)t\right) + \cos\left(\left(\omega_{c_r} - \omega_{c_l} - \omega_{r,u} + \omega_{l,v}\right)t\right)\right] \\
&\qquad + Z_{2,k} \left[\cos\left(\left(\omega_{c_r} + \omega_{c_l} + \omega_{r,u} + \omega_{l,v}\right)t\right) + \cos\left(\left(\omega_{c_r} + \omega_{c_l} - \omega_{r,u} - \omega_{l,v}\right)t\right)\right] \quad (102)
\end{aligned}$$

with the amplitudes

$$Z_{1,k} = \frac{A_r A_l}{2}\left(\omega_{c_r}^2 + 2k\omega_{c_r}\omega_{c_l} + \omega_{c_l}^2\right)$$

and

$$Z_{2,k} = -\frac{A_r A_l}{2}\left(\omega_{c_r}^2 - 2k\omega_{c_r}\omega_{c_l} + \omega_{c_l}^2\right).$$

Finally, the third cross component $\Psi_k^c(\alpha_r(t), \beta_l(t))$ is given for $r \neq l$ as

$$\begin{aligned}\Psi_k^c(\alpha_r(t), \beta_l(t)) &= \Psi_{k,r>l}^c(\alpha_r(t), \beta_l(t)) + \Psi_{k,l>r}^c(\alpha_r(t), \beta_l(t)) \\ &\approx \sum_{u=1}^{N_r}\sum_{v=1}^{N_l} -Z_{1,k}\left[\cos\left(\left(\omega_{c_r} - \omega_{c_l} - \omega_{r,u} - \omega_{l,v}\right)t\right) + \cos\left(\left(\omega_{c_r} - \omega_{c_l} + \omega_{r,u} + \omega_{l,v}\right)t\right)\right] \\ &\quad - Z_{2,k}\left[\cos\left(\left(\omega_{c_r} + \omega_{c_l} - \omega_{r,u} + \omega_{l,v}\right)t\right) + \cos\left(\left(\omega_{c_r} + \omega_{c_l} + \omega_{r,u} - \omega_{l,v}\right)t\right)\right] \quad (103)\end{aligned}$$

Hence, in presence of more than one bandpass signal additional spectral components occur arround $|\omega_{c_r} - \omega_{c_l}|$ and $\omega_{c_r} + \omega_{c_l}$. The frequency parts depend on the carrier frequencies of the bandpass signals. The spectral components are influenced by the weighting factor k. E.g., for the traditional TK operation ($k = 1$) the spectral component around $|\omega_{c_r} - \omega_{c_l}|$ dominates. In contrast for the modified TK operation ($k \neq 1$) additional relevant spectral components can be identified around $\omega_{c_r} + \omega_{c_l}$ making the usage of the frequency at twice the subband's center frequency $2\omega_c$ critical.

To verify the results a subband of bandwidth 625 MHz and carrier frequency 5.2 GHz is considered for $k = 1$. $K_S = 3$ bandpass signals of amplitudes $A_1 = 1$, $A_2 = 1/3$ and $A_3 = 2/3$, of bandwidths $B_1 = 5$ MHz, $B_2 = 10$ MHz and $B_3 = 1$ MHz as well as of carrier frequencies $f_{c_1} = 4.98$ GHz, $f_{c_2} = 5.04$ GHz and $f_{c_3} = 5.28$ GHz are assumed at the input of TK operation. Fig. 26 shows the positive frequency range for the resulting to one

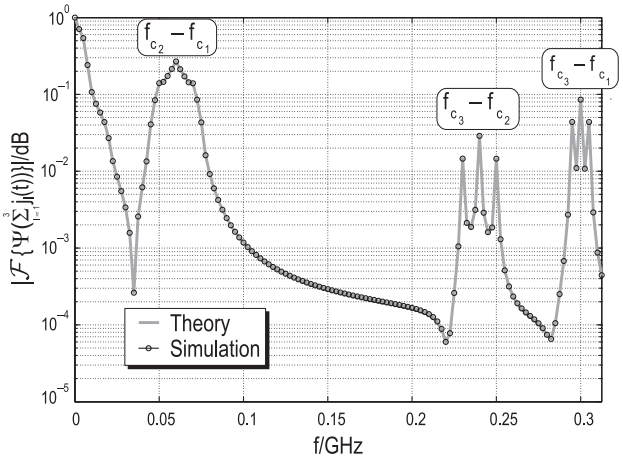

Figure 26. Normalized amplitude spectrum at the output of the traditional TK operation ($k = 1$) in presence of three narrowband bandpass signals.

normalized baseband spectrum at the output of the traditional TK operation. Simulation as well as analytical results show the spectral contributions of the three signals occurring at $f_{c_2} - f_{c_1} = 60$ MHz, $f_{c_3} - f_{c_2} = 240$ MHz and $f_{c_3} - f_{c_1} = 300$ MHz with the bandwidths 30 MHz, 22 MHz and 12 MHz. The spectral components are distributed over the complete bandwidth of the subband. For this reason the consideration of the TK operation with an additional filtering operation is critical. In particular, the mitigation scheme proposed in [42] becomes inefficient to efficiently mitigate all occurring interferences.

4.3.3. Integration of Teager-Kaiser operation

As illustrated in the previous section an integration of TK operation into the MIR-UWB system is possible with only minor complexity increase if at most one NBI occurs in each subband. In this case the approach of [42] can be used. It bases on the interplay of the TK operation with a highpass filtering. As illustrated in Fig. 27 only two additional analogue components have to be integrated into each subband of the existing non-coherent MIR-UWB receiver. Thereby, received subband signals are given to TK operation which acts as a frequency-to-DC shifter. The resulting low-frequency signal is afterwards highpass filtered to mitigate interfered signal components without any a priori information of the interference specific carrier frequency. As the bandwidth of the subband signal is larger than the interference bandwidth energy detection might be possible.

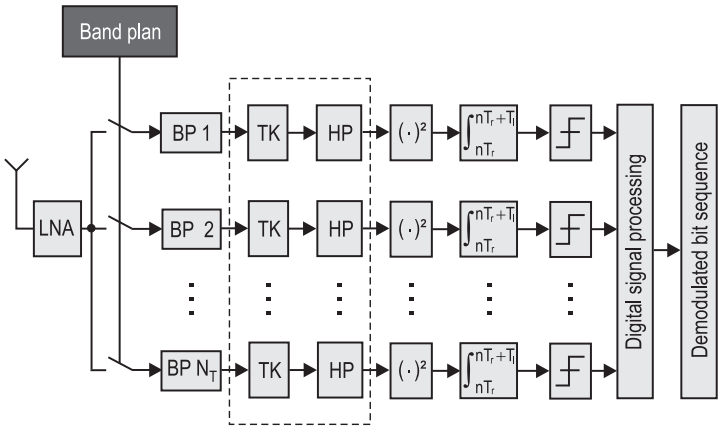

Figure 27. Integration of TK operation into the existing non-coherent MIR-UWB receiver.

In the following the potential of interference mitigation with the TK operation is shown for OOK in case of a binary one. An MIR-UWB subband of carrier frequency 5.13 GHz and effective bandwidth 162.5 MHz is considered for SNR $=$ 11 dB. It is assumed that an IEEE 802.11a WLAN signal [47] of bandwidth 20 MHz and of carrier frequency 5.14 GHz interferes the MIR-UWB subband with an SIR of -5 dB.

Fig. 28 (a) shows the to one normalized amplitude spectrum of all occurring signal components at the output of TK operation. Thereby, the UWB signal spectrum ranges from DC to 162.5 MHz whereas the lower frequency regions have a higher energy concentration. A similar behaviour occurs for the narrowband WLAN signal. Its corresponding amplitude spectrum ranges from DC to 20 MHz whereas energy is strongly distributed around DC. Furthermore, additional spectral cross components between signal, noise and interference occur which can be ascribed to the non-linearity of the TK operation. To mitigate the WLAN signal highpass filtering is done after the TK operation.

Fig. 28 (b) illustrates the to one normalized amplitude spectrum after highpass filtering. The used highpass filter is characterised by the order six, a passband ripple of 0.1 dB, a 50 dB stopband attenuation as well as a 50 MHz wide stopband. Obviously, the narrowband WLAN signal is mitigated after highpass filtering. In contrast the subband signal has an

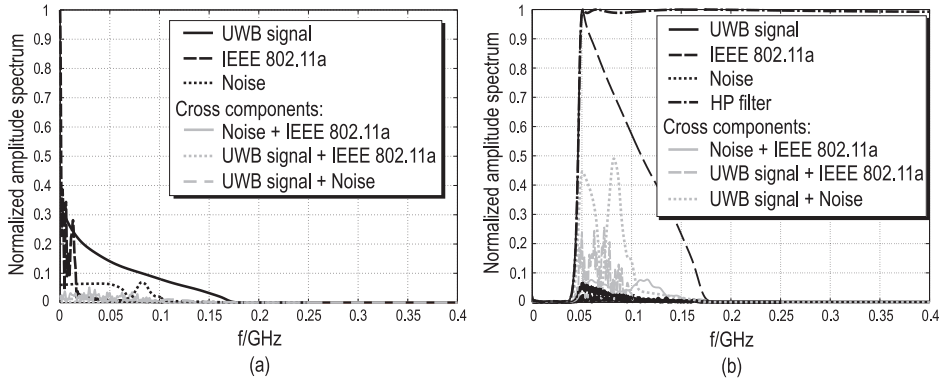

Figure 28. Normalized amplitude spectrum at the output of TK operation (a) and after highpass filtering (b), SNR = 11 dB.

amplitude spectrum which ranges from 50 MHz to 162.5 MHz. As this spectrum dominates the amplitude spectra of the occurring cross components energy detection is possible.

5. Summary

This chapter deals with an easy-to-realise non-coherent MIR-UWB system which is a promising approach for high data rate and energy efficient communication over short distances. Due to its low complexity the MIR-UWB system is an alternative to already existing UWB systems for high data rate applications such as Multiband OFDM UWB.

The MIR-UWB system is based on an energy detection receiver. Thus the first part of this chapter deals with the performance of this component. To understand the energy detection receiver we look at the bit and symbol error probability in different wireless channels.

First we introduce a closed form expression of the SEP for an energy detection receiver with M-PAM in the AWGN channel. Based on this result, we optimise the interval thresholds to minimise the SEP. Optimal interval thresholds guarantee a minimal SEP for M-PAM. In the next step we look into the optimal amplitudes for M-PAM using an energy detection receiver. This approach enables to reduce the SEP for M-PAM with medium to large degrees of freedom.

To understand the characteristics of the energy detection receiver in fading channels we look into different approaches to model the energy at the receiver. It has been shown, that the flat fading channel model can be used to model the energy at a receiver for a receiver bandwidth $B > 100$ MHz. Based on this assumption we introduce closed form expressions for the SEP of the energy detection receiver with M-PAM for different fading statistics such as *Rayleigh*, *Rice* and *Nakagami-m*. We also analyse the SEP of an multichannel receiver using different combining techniques. Square Law Combing and Square Law Selection are possible combining schemes for an energy detection receiver. A closed form solution for SLC and SLS is introduced for the AWGN and for the *Rayleigh* fading channel including i.i.d. and correlated fading gains.

The first part ends with the analysis of the SEP in a frequency selective fading channel. Based on *Rayleigh* distributed fading gains, representing a non line-of-sight channel (NLOS), we

introduce a closed form expression for the energy detection receiver with *M*-PAM. The result also contains the possibility to analyse the effect of correlated fading gains. This is the case in typical UWB wireless channels. If the fading gains are not *Rayleigh* distributed, we present a numerical solution for any fading distributions. The results of the first part enable a precise prediction of an energy detection receiver with *M*-PAM in many different scenarios.

Since the MIR-UWB system is highly sensitive to interference, the second part of the chapter considers three different aspects regarding an efficient interference mitigation.

The first aspect deals with the analysis of the interference robustness of an OOK and BPPM specific energy detection receiver being the essential component of the non-coherent MIR-UWB receiver. Thereby, taking into account thermal noise a general frame work is presented which can be used to give statements on the detector's interference robustness for an interference with arbitrary bandwidth. Furthermore, possible system parameters can be identified to increase the detector's interference robustness.

The second aspect considers the coexistence capability of the MIR-UWB system. Thereby, various easy-to-realise adaptive coexistence-based approaches are presented. Starting with a static coexistence approach a DAA coexistence approach for temporary NBI is presented being integrated into the system specific initialisation and data phase. The proposed method allows a reliable adaptive mitigation of temporary NBI. A further adaptive coexistence approach bases on image-based thresholding which can be integrated into the initialisation phase of the MIR-UWB system. Based on an exemplary interference scenario the potential to efficiently mitigate multiple interferences of different interference power is shown.

Lastly, the third aspect focuses on the analytical investigation of the potential to mitigate NBI inside an energy detection receiver. Hereby, the TK operation as well as a modified TK operation is analysed. It is shown that for a narrowband baseband signal the output of the TK operation is characterised by a larger energy concentration in the lower frequency range. In contrast, for the modified TK operation further spectral components occur for higher frequencies. A subsequent analysis of one NBI in the bandpass domain shows that the TK operation acts like a frequency-to-DC shifter. This reveals the potential to mitigate a single NBI without the knowledge of the NBI's carrier frequency. In contrast, for the modified TK operation additional spectral components at twice the NBI's carrier frequency occur making interference mitigation critical. In case of multiple NBI further spectral components occur at the TK operation's output which can be ascribed to the mutual interference influences. Due to a possible distribution of the spectral components within the total MIR-UWB subband interference mitigation depends on the interference position inside the MIR-UWB subband.

Acknowledgements

This work was supported within the priority program No. 1202 (UKoLoS) by the German Research Foundation (DFG).

Author details

Rainer Moorfeld and Adolf Finger
Communications Laboratory, Dresden University of Technology, Germany

Hanns-Ulrich Dehner, Holger Jäkel, Martin Braun and Friedrich K. Jondral
Communications Engineering Lab, Karlsruhe Institute of Technology (KIT), Germany

6. References

[1] Abramowitz, M. & Stegun, I. [1964]. *Handbook of mathematical functions with formulas, graphs, and mathematical tables*, Applied mathematics series, Dover Publications.

[2] Batra, A. [2008]. *Multiband OFDM Physical Layer Proposal for IEEE 802.15 Task Group 3a*, IEEE P802.15-03/268r1.

[3] Bober, M., Moorfeld, R. & Jorswieck, E. [2011]. Performance of Energy Detection in NLOS frequency-selective Fading Channels, *Proc. of IEEE International Symposium on Personal, Indoor and Mobile Communications (PIMRC)*.

[4] Cassioli, D., Win, M. Z. & Molisch, A. F. [2002]. The ultra-wide bandwidth indoor channel: from statistical model to simulations, *IEEE Journal on Selected Areas in Communications* 20(6): 1247–1257.

[5] Dehner, H., Jäkel, H., Burgkhardt, D. & Jondral, F. K. [2010]. The Teager-Kaiser Energy Operator in Presence of Multiple Narrowband Interference, *IEEE Communications Letters* Vol. 14(No, 8): 716 – 718.

[6] Dehner, H., Jäkel, H., Burgkhardt, D., Jondral, F. K., Moorfeld, R. & Finger, A. [2010]. Treatment of temporary narrowband interference in noncoherent multiband impulse radio UWB, *Proc. of IEEE Mediterranean Electrotechnical Conference*, pp. 1335 – 1339.

[7] Dehner, H., Jäkel, H. & Jondral, F. K. [2011a]. Narrow- and broadband Interference Robustness for OOK/BPPM based Energy Detection, *Proc. of IEEE International Conference on Communications*.

[8] Dehner, H., Jäkel, H. & Jondral, F. K. [2011b]. On the modified Teager-Kaiser energy operator regarding narrowband interference, *Proc. of IEEE Wireless Telecommunications Symposium*.

[9] Dehner, H., Koch, Y., Jäkel, H., Burgkhardt, D., Jondral, F. K., Moorfeld, R. & Finger, A. [2010]. Narrow-band Interference Robustness for Energy Detection in OOK/PPM, *Proc. of IEEE International Conference on Communications*.

[10] Dehner, H., Linde, M., Moorfeld, R., Jäkel, H., Burgkhardt, D., Jondral, F. K. & Finger, A. [2009]. A low complex and efficient coexistence approach for non-coherent multiband impulse radio UWB, *Proc. of IEEE Sarnoff Symposium*.

[11] Dehner, H., Moorfeld, R., Jäkel, H., Burgkhardt, D., Finger, A. & Jondral, F. K. [2009]. Multi-band Impulse Radio – An Alternative Physical Layer for High Data Rate UWB Communication, *Frequenz, Journal of RF-Engineering and Telecommunications* Vol. 63(No, 9-10): 200–204.

[12] Dehner, H., Romero, A., Jäkel, H., Burgkhardt, D., Moorfeld, R., Jondral, F. K. & Finger, A. [2009]. Iterative coexistence approaches for noncoherent multi-band impulse radio UWB, *Proc. of IEEE International Conference on Ultra-Wideband*, pp. 734 – 738.

[13] Digham, F. F., Alouini, M.-S. & Simon, M. K. [2007]. On the Energy Detection of Unknown Signals Over Fading Channels, *IEEE Transactions on Communications* 55(1): 21–24.

[14] ECC [2006]. ECC decision of 24 march 2006 on the harmonised conditions for devices using ultra-wideband (UWB) technology in bands below 10.6 GHz, *Technical Report* .

[15] Eisenacher, M. [2006]. Optimierung von Ultra-Wideband-Signalen (UWB), *Dissertation, Forschungsberichte aus dem Institut für Nachrichtentechnik der Universität Karlsruhe (TH), Band 16, 2006* .

[16] Fisher, R., Kohno, R., Laughlin, M. & Welborn, M. [2005]. *DS-UWB Physical Layer Submission to 802.15 Task Group 3a*, IEEE P802.15-04/0137r1.
[17] Ghassemzadeh, S. S., Jana, R., Rice, C. W., Turin, W. & Tarokh, V. [2004]. Measurement and modeling of an ultra-wide bandwidth indoor channel, *IEEE Transactions on Communications* 52(10): 1786–1796.
[18] Gradshteyn, I. S. & Ryzhik, I. M. [2007]. *Table of Integrals, Series, and Products*, 7 edn, Academic Press.
[19] Hentilä, L., Taparungssanagorn, A., Viittala, H. & Hämäläinen, M. [2005]. Measurement and modelling of an UWB channel at hospital, *Proc. of IEEE International Conference on Ultra-Wideband (ICU)*.
[20] Hovinen, V., Hämäläinen, M. & Pätsi, T. [2002]. Ultra wideband indoor radio channel models: preliminary results, *IEEE Digest of Papers Ultra Wideband Systems and Technologies*.
[21] Johnson, N. L., Kotz, S. & Balakrishnan, N. [1994]. *Continuous Univariate Distributions*, Vol. 1, 2 edn, Wiley.
[22] Kaiser, J. [1990]. On a simple algorithm to calculate the energy of a signal, *Proc. of IEEE International Conference on Acoustics, Speech, and Signal Processing*, pp. 381 – 384.
[23] Kaiser, J. [1993]. Some Useful Properties of Teager's Energy Operators, *Proc. of IEEE International Conference on Acoustics, Speech, and Signal Processing*, pp. 149 – 152.
[24] Karedal, J., Wyne, S., Almers, P., Tufvesson, F. & Molisch, A. F. [2004]. Statistical analysis of the UWB channel in an industrial environment, *Proc. of IEEE Vehicular Technology Conference (VTC-Fall)*.
[25] Kay, S. M. [1998]. *Fundamentals of Statistical Signal Processing: Detection Theory*, Vol. 2, Prentice Hall.
[26] Kunisch, J. & Pamp, J. [2002]. Measurement results and modeling aspects for the UWB radio channel, *IEEE Digest of Papers Ultra Wideband Systems and Technologies*.
[27] Lee, W. C. [1997]. *Mobile Communications Engineering: Theory and Applications*, McGraw-Hill, Inc.
[28] Li, L., Moorfeld, R. & Finger, A. [2011a]. Bit and power loading for the multiband impulse radio UWB architecture, *Proc. of 8th Workshop Positioning Navigation and Communication (WPNC)*.
[29] Li, L., Moorfeld, R. & Finger, A. [2011b]. Closed form expressions for the symbol error rate for non-coherent UWB impulse radio systems with energy combining, *Proc. of 8th Workshop Positioning Navigation and Communication (WPNC)*.
[30] Mittelbach, M., Moorfeld, R. & Finger, A. [2006]. Performance of a Multiband Impulse Radio UWB Architecture, *Proc. of 3rd International conference on mobile technology, applications and systems*.
[31] Molisch, A. F., Cassioli, D., Chong, C.-C., Emami, S., Fort, A., Kannan, B., Karedal, J., Kunisch, J., Schantz, H. G., Siwiak, K. & Win, M. Z. [2006]. A comprehensive standardized model for ultrawideband propagation channels, *IEEE Transactions on Antennas and Propagation* 54(11): 3151–3166.
[32] Molisch, A. F., Foerster, J. R. & Pendergrass, M. [2003]. Channel models for ultrawideband personal area networks, *IEEE Wireless Communications Magazine* 10(6): 14–21.
[33] Moorfeld, R. & Finger, A. [2009]. Multilevel PAM with optimal amplitudes for non-coherent energy detection, *Proc. of Wireless Communications and Signal Processing (WCSP)*.

[34] Moorfeld, R., Finger, A., Dehner, H., Jäkel, H. & Jondral, F. K. [2008]. A simple and fast detect and avoid algorithm for non-coherent multiband impulse radio UWB, *Proc. of IEEE International Symposium on Spread Spectrum Techniques and Applications*, pp. 587 – 591.

[35] Moorfeld, R., Finger, A., Dehner, H.-U., Jäkel, H. & Jondral, F. K. [2009]. Performance of a high flexible non-coherent multiband impulse radio UWB system, *Proc. of 9th IASTED International Conference on Wireless and Optical Communications (WOC)*.

[36] Moorfeld, R., Finger, A. & Zeisberg, S. [2004]. High data rate UWB performance with reduced implementation complexity, *Proc. of IEEE International Symposium on Spread Spectrum Techniques and Applications (ISSSTA)*.

[37] Moorfeld, R., Lu, Y. & Finger, A. [2012]. Energy detection with optimal symbol constellation for M-PAM in UWB fading channels, *Proc. of IEEE International Conference on Ultra-Wideband (ICUWB)*.

[38] Moorfeld, R., Zeisberg, S., Pezzin, M., Rinaldi, N. & Finger, A. [2004]. Ultra-Wideband Impulse Radio (UWB-IR) Algorithm Implementation Complexity and Performance, *Proc. of IST Mobile and Wireless Communications Summit*.

[39] Nuttall, A. H. [1972]. Some integrals involving the Q function, *Technical report*, Naval Underwater Systems Center (NUSC).

[40] Nuttall, A. H. [1975]. Some integrals involving the Q_M function, *IEEE Transactions on Information Theory* 21(1): 95–96.

[41] Otsu, N. [1979]. A threshold selection method from gray-level histograms, *IEEE Transactions on Systems, Man, and Cybernetics* Vol. 20: 62 – 66.

[42] Ozdemir, O., Sahinoglu, Z. & Zhang, J. [2008]. Narrowband Interference Resilient Receiver Design for Unknown UWB Signal Detection, *Proc. of IEEE International Conference on Communications*, pp. 785 – 789.

[43] Pagani, P. & Pajusco, P. [2006]. Characterization and Modeling of Temporal Variations on an Ultrawideband Radio Link, *IEEE Transactions on Antennas and Propagation* 54(11): 3198–3206.

[44] Papoulis, A. [2002]. *Probability, Random Variables and Stochastic Processes*, 4. edn, McGraw-Hill.

[45] Paquelet, S. & Aubert, L. M. [2004]. An energy adaptive demodulation for high data rates with impulse radio, *Proc. of IEEE Radio and Wireless Conference*, pp. 323–326.

[46] Paquelet, S., Aubert, L. M. & Uguen, B. [2004]. An impulse radio asynchronous transceiver for high data rates, *Proc. of Joint Conference on Ultrawideband Systems and Technologies Ultra Wideband Systems (UWBST & IWUWBS)*.

[47] *Part 11: Wireless LAN Medium Access Control (MAC) and Physical Layer (PHY) Specifications: High-speed Phyiscal Layer in the 5 GHz Band* [1999]. IEEE Std. 802.11a-1999.

[48] Press, S. J. [1966]. Linear combinations of non-central chi-square variates, *The Annals of Mathematical Statistics* 37(2): 480–487.

[49] Proakis, J. G. [2001]. *Digital Communications*, 4th edn, McGraw-Hill.

[50] Rappaport, T. S. [2002]. *Wireless Communications: Principles and Practice*, Prentice Hall.

[51] Saleh, A. A. M. & Valenzuela, R. [1987]. A statistical model for indoor multipath propagation, *IEEE Journal on Selected Areas in Communications* 5(2): 128–137.

[52] Simon, M. K. & Alouini, M.-S. [2006]. *Digital Communication over Fading Channels: A Unified Approach to Performance Analysis*, Wiley.

[53] Steiner, C. & Wittneben, A. [2007]. On the interference robustness of ultra-wideband energy detection receivers, *Proc. of IEEE International Conference on Ultra-Wideband*.

[54] Stoica, L. [2008]. *Non-coherent energy detection transceivers for Ultra Wideband Impulse radio systems*, PhD thesis, Centre for Wireless Communications, Oulu, Finland.
[55] Tse, D. & Viswanath, P. [2005]. *Fundamentals of wireless communication*, Cambridge University Press.
[56] Urkowitz, H. [1967]. Energy detection of unknown deterministic signals, *Proc. of the IEEE* 55(4): 523–531.
[57] Weiß, T. [2004]. OFDM-basiertes Spectrum Pooling, *Dissertation, Forschungsberichte aus dem Institut für Nachrichtentechnik der Universität Karlsruhe (TH), Band 13* .
[58] Witrisal, K., Leus, G., Janssen, G., Pausini, M., Troesch, F., Zasowski, T. & Romme, J. [2009]. Noncoherent ultra-wideband systems, *IEEE Signal Processing Magazine* Vol. 26(No, 4): 48 – 66.
[59] Zhang, H., Udagawa, T., Arita, T. & Nakagawa, M. [2002]. A statistical model for the small-scale multipath fading characteristics of ultra wideband indoor channel, *Proc. of IEEE Digest of Papers Ultra Wideband Systems and Technologies*.
[60] Zhao, L. & Haimovich, A.-M. [2002]. Performance of ultra-wideband communications in the presence of interference, *IEEE Journal on Selected Areas in Communications* Vol. 20(No, 9): 1684 – 1691.